Lunds Universitets Naturgeografiska Institution

Seminarieuppsatser Nr. 61

Variations in the Energy Budget above Growing Wheat and Barley, Ilstorp 1998

- a gradient-profile approach

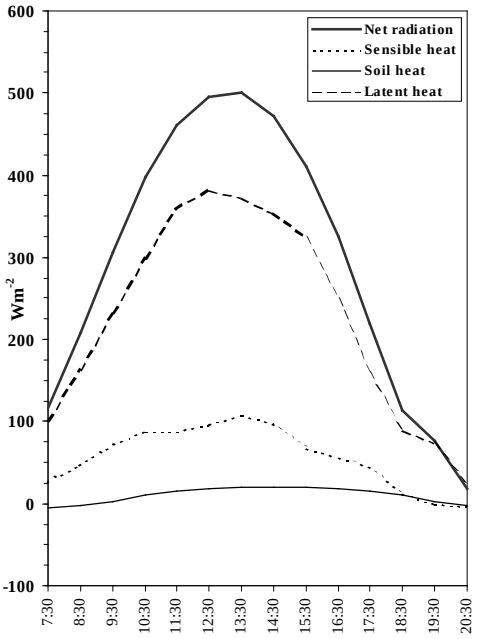

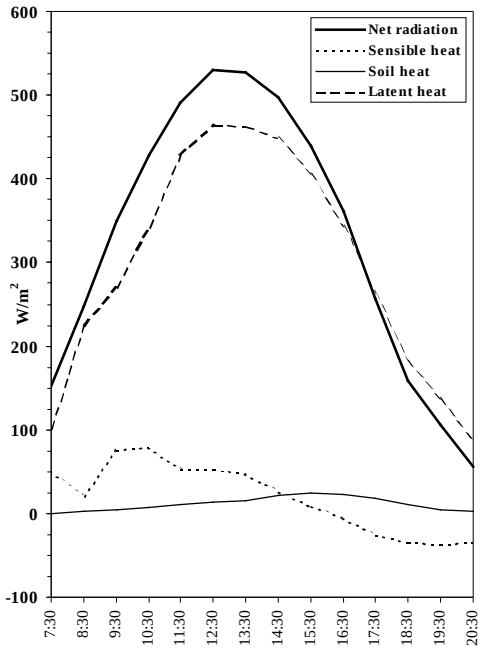

Surface energy budget on the 16th of May. *Surface energy budget on the 21st of June.*

Carin Kjellander

Department of Physical Geography,
Lund University
Sölvegatan 13, S-221 00 Lund,
Sweden

1999

Abstract

Fluxes of sensible heat and latent heat were calculated above fields of barley and wheat in Ilstorp, using a gradient profile approach. Gradient Richardson's number was used as the stability parameter, and it was shown that atmospheric stability varies both with time of the day and wind speed. Temperature and wind profiles were studied, and it was possible to detect a rise in the active surface in relation to increasing crop height. Displacement heights and roughness lengths were calculated for separate periods of time. The connection between these parameters and crop height was perhaps not as simple as predicted.

The results were used to estimate the energy budget above growing crop; encompassing net radiation, sensible heat, latent heat and soil heat fluxes. It was found that, in the beginning of the season, latent heat flux dominated the energy balance budget. As the crop matured and turned yellow, crop height decreased slightly, and the sensible heat flux now increased above the latent heat flux. Soil heat flux remained quite constant during the summer, around 0 to 15 W m^{-2}.

Acknowledgement

I would like to thank my supervisor Lars Bärring for taking a keen interest in my work, patiently providing me with good general advice and support, blended with detailed comments and valuable hints!

I would also like to thank Peter Jönsson for helping me to structure my essay, and organise the field work.

Further, I would like to thank all the people who have been involved in my work, and helped me with various different steps on the way to complete my report: Zinaida Iritz, Maj-Lena Lindersson, Christine Aschberger, Marie Ekström, Harry Lankreijer, Christian Svensson, Sten Stenbeck, Hans Ahlmann, Peter Nordström, Sasha Sedletski, Charlotte Kjellander and Martin Nilsson.

A special acknowledgement should be made to Ulf Jacobsson and Tomas Henriksson, who let me place my instruments in their fields during the measuring season. Thank you!

CONTENTS

1. INTRODUCTION

Life on earth may be seen as constantly triggered by the transformation of solar energy into countless energy components, nurturing the global earth-surface system of biological, geological and atmospheric processes. These processes, in turn, generate flows of sensible heat and latent heat, giving rise to an endless metamorphosis of energy, disguised in wind and fluxes of heat and water vapour. This report will focus on the energy fluxes in the atmosphere at the near surface level above cultivated fields.

Research of the interactive processes in the earth-surface system involves studies of the fundamental energy and water cycles, including the processes by which mass and energy is transferred, converted and stored. The basic energy flux components in an earth-surface system have been outlined by Miller (1981) as encompassing absorbed solar (short-wave) and long-wave radiation, the photosynthetic conversion of solar energy, the release of energy from fossil sources as well as from decomposition, thermal energy emitted by leaves, energy temporarily stored in the ground, sensible and latent heat fluxes from the surface into the air, and conversions of kinetic and potential energy, such as wind energy.

Together these components form the basis of the energy balance of an earth-surface system, with energy inputs and outputs at equilibrium. At the surface in a closed system this equilibrium can be explained by an energy balance equation. Several studies in microclimatology have used this energy balance approach to further investigate the fluxes of energy above different types of surfaces such as agricultural fields and forests, for example soybeans and maize (Hicks and Wesely, 1981), wheat (Huband and Monteith, 1986a, 1986b), deciduous forest (Verma *et al.*, 1986) and short-rotation willow (Lindroth and Iritz, 1993).

Earlier studies of energy fluxes have focused on methods based on the flux-profile relationship where the vertical distribution of wind, temperature and humidity are used to estimate flow of momentum, sensible and latent heat. The first empirical flux-profile relationship to be used, according to Yaglom (1977) was developed by Monin and Obukohov in the early 1950´s as a universal function of the wind velocity profile. Before them, in 1942, Thornthwaite and Holzman had used the aerodynamic approach to determine evapotranspiration (Rosenberg *et al.*, 1983).

When using the flux-profile method, care has to be taken to include the role of the atmospheric condition, since the relation is built on the logarithmic wind profile equation, which only is applicable for neutral thermal stratification. This complication has been solved in different ways during time. In a review of the flux-profile relationships Dyer (1974) comments on the measures of stability in use; the gradient Richardson's Number, used by Sutton in 1953, and the later Obukhov length developed by Monin and Obukhov. The refinement of sensors and instrumentation has encouraged the use of the Obukhov length, which requires measurements of sensible heat flux and friction velocity, whereas Richardson's Number only needs data from the more easily measured wind and temperature gradients.

Since the flux-profile method is valid only for neutral atmospheres, an additional step has to be taken to include other types of atmospheric stability, once the thermal stability has been derived. Hence, in a stable or unstable atmosphere the flux-profile method make use of stability exchange coefficients, which were developed during the 1970´s. Thom *et al.* (1975) further discussed the use of exchange coefficients in unstable atmospheres above pine forest.

The wind profile, which the flux-profile method is based on, is sensitive to the environmental surroundings. The smoothness of the surface, above which the flux-profile relation is utilised, is

an important parameter, as well as the fetch. In a study by Grant (1994) the wind profiles through the stable boundary layer was presented, and it became clear that a nearby ridge (2 to 3 km from the measuring site) influenced the wind direction in particular, but also effected the wind speed at the investigation site. Already Cellier (1986) had questioned the applicability of the flux-profile relationship above very rough surfaces, such as for example savannah and coniferous forest. The rule of thumb is to have a fetch which is ten to thirty times greater in magnitude than the highest measuring point (Oke, 1987).

Other parameters to effect the wind profile include vegetation height, zero plane displacement height and roughness length. Panofsky (1963) made a detailed attempt in showing how to derive these factors from measured data.

The areas of practical application for knowledge in energy fluxes are diverse. Several attempts have been made to model energy fluxes above vast areas, for example to predict crop yields in African Sahel and Southern France (Lagouarde and McAneney, 1992), or to improve the parameterisation of land surface processes in general circulation models (Lhomme *et al.*, 1994; Blümel, 1998). On a smaller scale, studies of the energy balance have been made to estimate evaporation rates from wheat canopies (Huband and Monteith, 1986a, 1986b), and evapotranspiration in vineyards (Trambouze *et al.*, 1998). Results from flux-profile relations in combination with the energy balance equation have gradually expanded to include discussions on fluxes of water vapour and carbon dioxide within agricultural crops or forests (Verma *et al.*, 1986). Differences in energy balance observations have also been used as a measure of the impact of urban development at a rural and a suburban site in Vancouver (Cleugh and Oke, 1986).

2. AIM OF STUDY

This study is concerned with the microclimate at and near the surface, with datasets extending from a depth of 0.10 m into the ground to 10 m above the ground. The climate in this limited region is predominantly a result of the exchange and flux of energy. Fluxes of energy will be derived using an aerodynamic gradient-profile approach, based on the theory of the logarithmic wind profile, and the assumption of similarity between the diffusion transfer coefficients for momentum, sensible heat and latent heat. The theme is to provide a description of the micro climatological processes present, above and within two fields of wheat and barley by studying the seasonal and diurnal variations in wind profiles, temperature profiles and atmospheric stability and then quantifying the energy budget components.

The specific aim of the study is to show

- the relation between **increasing crop height** and **the logarithmic wind profile**,
- the relation between **increasing crop height** and **temperature profiles**,
- the diurnal and seasonal variation of **atmospheric stability**,
- the relation of **increasing crop height** and **fluxes of sensible and latent heat**, and
- the **diurnal and seasonal variation in the energy balance**.

The study of energy fluxes will not include the photosynthesis and the flow of carbon dioxide, which constitutes 2 – 5 % of the total energy budget (Oke, 1987), but will concentrate on the sensible heat, latent heat and soil heat fluxes.
The period of study is restricted to the growing season of 1998.
Wind profiles and temperature profiles have been produced for both fields separately, but due to limitations in availability of instruments the energy balance components have been calculated for the two fields together.

3. THEORY:
SURFACE LAYER CLIMATES ABOVE AGRICULTURAL FIELDS

3.1 THE RADIATION BALANCE

The amount of radiative energy input and output, adding up to a steady level of net energy loss and net energy gain per day at the earth surface, can be simplified by the equation;

$$Q^* = Q\downarrow - Q\uparrow \tag{3.1}$$

Q^* is the net radiative total energy. $Q\uparrow$ represents energy leaving the earth surface, whereas $Q\downarrow$ symbolizes the incoming radiative energy from the sun. These energy components can be divided into two main categories, based on wavelength. The solar radiation, or short wave radiation, is set to include wavelengths in the range 0.15 – 3.0 μm, and thermal radiation from the earth and the clouds, long wave radiation, has wavelengths in the range of 3.0 - 100 μm (Oke, 1987). The energy equation (3.1) above may be expanded to specify the directions of the long and short wave radiation. During the day it holds that the net energy, Q*, is the sum of net short wave radiation (K*) and the net long wave radiation (L*). The net short wave radiation, in turn, is the difference between the incoming (K↓) and the reflected short wave radiation (K↑). Equally, the net long wave radiation is comprised of thermal radiation from the earth (L↑) as well as reflected and emitted long wave radiation from clouds and particles (L↓). The extension of equation (3.1) then becomes;

$$Q^* = K^* + L^* = (K\downarrow - K\uparrow) + (L\downarrow - L\uparrow) \tag{3.2}$$

In general, some of the incident short-wave solar radiation will be reflected by the earth surface, while the rest will be absorbed by the earth and penetrate downwards as sensible heat. Applying the law of conservation of energy, the ratios of reflected, absorbed and transmitted energy of a particular wave length should summarize to equal unity (Oke, 1987). At night, when no sunlight is present, the net radiation reduces to be explained by the net long wave radiation only.
The portion of reflection depends on the albedo (α) of a particular surface, which is expressed by equation (3.3).

$$K\uparrow = K\downarrow(\alpha) \tag{3.3}$$

K↑ represents the reflected short wave radiation, and K↓ stands for the direct and diffuse solar radiation. For soils the value of the albedo stretches from 0.05 for very dark moist soils to around 0.40 for light dry soils (Oke, 1987). Albedo for agricultural crops range between 0.18 and 0.25.

The amount of solar energy that reaches the earth's surface is determined by a number of factors including the intensity of the radiation emitted by the sun, the inclination angle on the earth of the sun rays, and the general transparency of the air such as the degree of cloudiness and turbidity (Rosenberg *et al.*, 1983). The radiation intensity at the top of the atmosphere, the solar constant, amounts to around 1370 Wm^{-2} (Oke, 1987, p.18; Stull, 1988, p. 257) given that the earth is at the mean distance from the sun. The season and time of day then determine the inclination angle, the angle at which the radiation will be incident on the earth surface. The transparency of the air is influenced by the extent of clouds and by the size and number of aerosol particles in suspension present. Cirrus clouds will have the least impact on incoming

radiation, middle clouds have a higher influence and low stratus clouds strongly reduce incoming radiation (Rosenberg *et al*., 1983).
The long-wave radiation, emitted by the earth surface, the clouds and the atmosphere, depends on temperature and emissivity. Emissivity is defined as "*the ratio of the total radiant energy emitted per unit time per unit area of a surface at a specified wavelength and temperature to that of a blackbody under the same conditions"* (Oke, 1987, p. 401). The amount of incoming long-wave radiation from clouds and atmosphere can be explained by including emissivity, ε, into the Stefan-Boltzmann Law, so that:

$$L\downarrow = \varepsilon\sigma T^4 \tag{3.4}$$

The Stefan-Boltzmann constant, σ, equals 5.67×10^{-8} W m^{-2} K^{-4}, and T is the body surface temperature in Kelvin. The radiation from the earth surface is also explained by equation (3.4), but in order to get the total amount of outgoing long-wave radiation, L↑, the portion of reflected long-wave radiation need to be included. With Kirchoff´s Law, stating that bodies which are good absorbers are also good emitters (given the same temperature and wavelength) the reflectivity of a surface expressed as unity minus absorption, can also be described as unity minus emissivity. The total L↑ can then be written as:

$$L\uparrow = \varepsilon\sigma T^4 + (1-\varepsilon)L\downarrow \tag{3.5}$$

To give an example a study above a barley field in Rothamsted, England (Oke, 1987) on the 23rd of July, 1963, found that the short-wave radiation peaked at just below 800 Wm^{-2} at noon, and the amount of reflected short-wave radiation reached to around 170 W m^{-2}. The net long wave radiation showed less of great amplitude in the diurnal cycle, oscillating from 0 to approximately 70 W m^{-2} during the day.

3.2 THE SURFACE ENERGY BALANCE

Net radiation, Q*, serves as the basic input to the energy surface balance. Thus it is partitioned into sensible heat (Q_H), latent heat (Q_E) and heat conduction in the soil (Q_G) (Oke, 1987).

$$Q^* = Q_H + Q_E + Q_G \tag{3.6}$$

The physical properties of the surface, and the relative ability of the soil and atmosphere to transport heat, determine in what form the energy leaves the surface, i. e. the fractions of Q_H, Q_E and Q_G (Oke, 1987). Slightly more detailed, the ability of vertical and horizontal heat transportation in the surface layer is related to the viscous properties of air and the transfer of momentum associated with viscous forces (Monteith and Unsworth, 1990).

3.3 TRANSPORT OF ENERGY FLUXES

3.3.1 Air flow, momentum and surface shearing stress

The motion of wind over a flat surface is often compared to the motion of fluids in a pipe-like container or a tunnel. When a fluid of a certain viscosity flows through a pipe, the walls of the pipe will effect the flow velocity of the fluid. If a transect is taken at right angle of the flow in the pipe, it can be seen that the speed of the fluid at the centre of the pipe is higher than the speed closer to the pipe walls. The flow velocity at the actual wall is zero. Hence the pipe walls exert a resistance to the passage of the fluid.

Taking the analogy of fluids in pipes to explain the behaviour of wind blowing over a flat surface, the ground can be seen as the pipe wall, which drags down the wind speeds at low heights. This dragging force is referred to as the surface shearing stress (τ) (Oke, 1987; Rosenberg *et al*., 1983), and may equally be explained as the force exerted on the surface by the wind.

At slow speeds the flow in a pipe can be imagined to consist of several layers, or lanes (if viewed only in two dimensions), each one with a traffic of molecules moving just a little faster than in its neighbour lane closer to the wall. These lanes would be totally independent of one another, were the fluid molecules moving exactly in straight lines after each other through the pipe, like cars on a highway with thick lines in between the lanes. This kind of flow is said to be laminar, and occur at a very small scale just above the earth surface.

However, the molecules in a fluid might move in all directions, and then interfere with its neighbour layers. A molecule from a faster layer might roam into a layer of slower speed, and then bring a higher momentum into the slower layer. This transfer of momentum across the layer borders quickens the slower layers, which in turn drag down the speed in the faster layers.

In general, laminar flow is only found in a very thin layer of a few millimetres above smooth surfaces. Instead turbulent flow is dominant in the atmosphere. Turbulence can be described as a state of motion of a fluid in which the velocity shows fluctuations of a random character, and it is the mechanism by which the transfer of momentum as well as sensible heat fluxes in the atmosphere occurs. The transfer is done through turbulent eddies which move in a three-dimensional manner, while conserving temperature, momentum and water vapour. The eddies can be of various sizes and move from one stream to another. The velocity of the eddies increases with height above ground. Close to the earth surface the eddies are slow, and if such a slow eddy moves upwards into a new height it causes a lull when it imparts its lower velocity into the mean velocity at the new height. In analogy with the discussion above a descending eddy brings its higher velocity down to the mean velocity at a lower height, causing a gust.

3.3.2 The logarithmic wind profile

The surface shearing stress, τ, effects the wind speed in such a way that close to the ground, where small eddies are present, low wind speeds prevail (Rosenberg *et al*., 1983). With an increase in height, in the first few meters above ground, there is a large increase in wind speed relative to the wind speed at lower levels (figure 3.1 (a)).

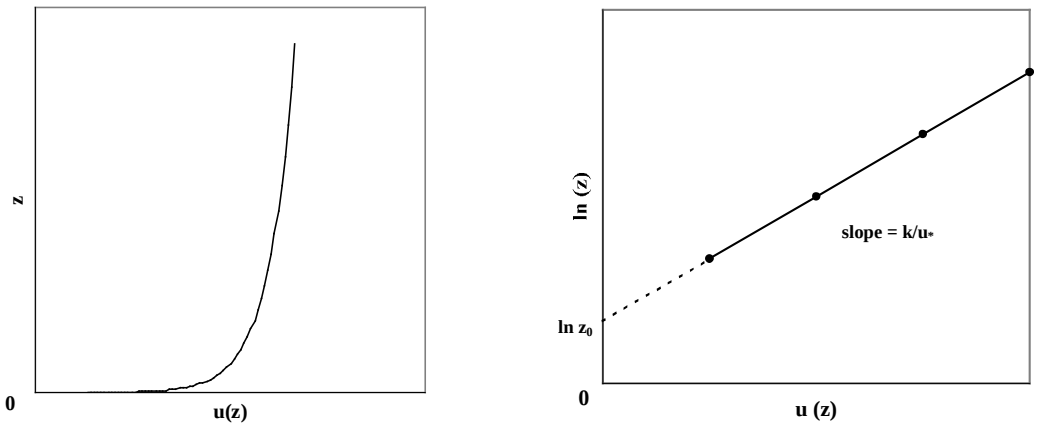

Figure 3.1 (a) and (b). Representative wind profiles above a smooth surface, where wind speed is plotted against height (z) in (a), and in (b) plotted against the natural logarithm of z. The line in (b) has been extended to the interception with the y-axis, where the roughness length (z_0) is found. The slope of the line in (b) is explained by von Karman's constant (k) divided by the friction velocity (u_*).

The shape of the curve have been found to coincide with the logarithmic decay curve, in such a manner, that if the natural logarithm of height (ln z) is used as the vertical axis and mean wind speed is shown along the horizontal axis, the data fall on a straight line (figure 3.1(b)). The equation describing the line is known as the logarithmic wind profile:

$$u(z) = \frac{u_*}{k} \ln \frac{z}{z_0} \qquad \text{m s}^{-1} \tag{3.7}$$

In equation (3.7) u(z) represents the mean wind speed (m s^{-1}) at height z (m), with k as von Karman's constant, u_* as the friction velocity (m s^{-1}) and z_0 as the roughness length (m) (Oke, 1987). These last parameters will be discussed in the next sections.

3.3.3 Friction velocity (u_*)

Friction velocity, u_*, can be seen to represent the effect of shearing stress, τ, on the ground (Kaimal and Finnigan, 1994). By finding u_* from the logarithmic wind profile, using the slope in figure 3.1.(b), and ρ as the density of air, the shearing stress can be found through equation;

$$\tau = \rho u_*^2 \tag{3.8}$$

3.3.4 Roughness length (z_0) and zero plane displacement height (d)

The roughness length, z_0 (or more visually expressed: the roughness height) of a surface describes the hypothetical height at which the elongated straight line from a wind profile, plotted against the logarithmic height, cuts the y-axis (where wind speed equals zero)(figure 3.1(b)). It is a measure of the level where the wind speed mathematically would be zero, due to the roughness of the surface. (Rosenberg *et al*., 1983)

During the growing season, when the crop height successively increases, the logarithmic wind profile is equally effected. The crop stand is noted to displace the wind profile vertically so that

a hypothetical surface is developed at the height of about two thirds of the crop height (Oke, 1987). This imaginary surface is called the displacement height, *d*, and it allows the logarithmic wind profile to be applicable to rough vegetated surfaces as well as to non-vegetated smooth surfaces (figure 3.2).

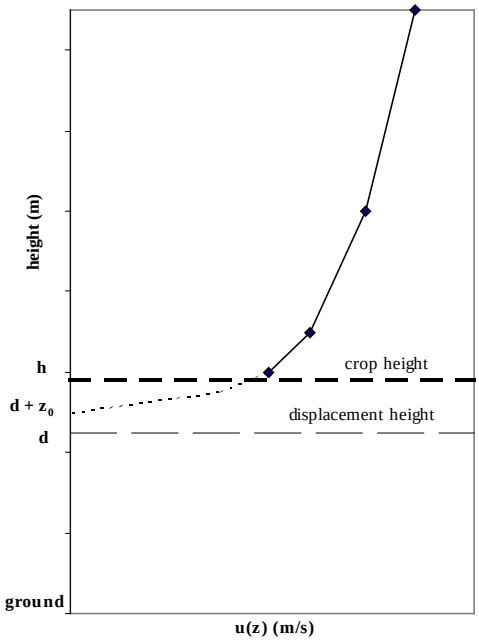

Figure 3.2. A typical wind profile above growing crop, with crop height h (m). The zero plane displacement height, d, rises to roughly 2/3 of the crop height. The extrapolated line shows the theoretical height (d + z_0) at which wind speed equals zero.

When the wind speeds at different heights over a crop are plotted in a diagram, the y-axis (height in m) is cut by the elongated wind profile over the crop at the height of $d + z_0$, instead of just z_0 (figure 3.2). The logarithmic wind profile equation (3.7) should hence be modified accordingly:

$$u(z) = \frac{u_*}{k}\ln\left(\frac{z-d}{z_0}\right) \qquad \text{m s}^{-1} \qquad (3.9)$$

Below the level $d + z_0$ the turbulence is strongly reduced, whereas above the hypothetical $d + z_0$ level the air is actively turbulent. Theoretically the level at $d + z_0$ is an equivalent height for zero wind speed, and d is the height at which momentum is received. (Monteith and Unsworth, 1990)

The relation between roughness length, displacement height and crop height has been discussed in several studies. Hicks and Wesely (1981) have done a comparison of heat flux above fields of soybeans and maize, in Sangamon, Illinois, where they have measured the roughness length and zero plane displacement height for the two crops. It was found that, for the soybean canopy, the momentum displacement height was located at close to 90 % of the total crop height, and the roughness length was about 5 % of the crop height. In the field of maize the displacement height was measured to be about 60 % of the crop height, and the roughness length about 7%.

Mölder (1998) have determined displacement height and roughness length above fields of barley, in Tamme and Tõravere, Estonia, and tall grass in Lövsta, Sweden. The displacement height at the sites of barley constituted ¾ and $^2/_3$ of crop height, and the tall grass had a displacement height of ¼ of crop height. The roughness length for barley, Tamme, was 0.075 of crop height, and at the other two sites it was 0.1, and 0.11 of the roughness length. However, the general approximation of z_0 and d for field crops implies that d ~ 2/3 crop height, and z_0 ~1/10 crop height (Oke, 1987).

The logarithmic wind profile discussed above requires a very important criterion to be fulfilled: the logarithmic wind profile is strictly valid for atmospheric conditions of neutral stability only.

3.4 ATMOSPHERIC STABILITY

3.4.1 Forced and free convection

A great portion of energy is transferred from the surface to the air by vertical movements of so called air parcels. These convective forces form two different groups; forced convection and free convection.

Forced convection indicates that motion in the air is caused by mechanical forces, such as friction of the air flow against the surface, or the wind, whereas free convection prevails when there is a density difference in the air. If still air lies just above a warm surface, for example, the air will be heated, and start to rise, due to increased buoyancy (Rosenberg, *et al*., 1983).

It is this flow, by free or forced convection, of energy, in the form of sensible heat, which is termed sensible heat flux. The convective activity is often revealed by using the vertical temperature profile as expressed in the concept of stability.

3.4.2 Lapse rates and stability

The concept of stability refers to the movement of air parcels which depends on the distribution of temperature with height. In neutral stability, with unsaturated air, the temperature decreases with height according to the dry adiabatic lapse rate, 0.98 K/100 m (Stull, 1995). This means that any vertical movement of an air parcel and its corresponding cooling (or heating) will remain in equilibrium with the surrounding air. In the case of atmospheric unstability, the air temperature decreases faster with height than the dry adiabatic lapse rate. An air parcel, which starts to rise during unstable conditions, will follow the dry adiabatic lapse rate, and hence find itself warmer than the surrounding air at a point higher up above the ground. This will cause the parcel to keep on rising and expanding. The reverse can be noted for the stable stratification. If an air parcel is forced upwards by wind, for example, it will cool along a line parallel to the dry adiabatic lapse rate. At its new higher position it will be cooler than the surrounding air temperature, and hence strive to sink.

As mentioned earlier, Dyer (1974) has presented a comparison of flux-profile relationships. One way to determine the atmospheric stability is by using the Obukohov length. That approach can be used provided that data on temperature flux at the surface and friction velocity is available. This study will use the more widely used indicator of stability in early atmospheric work, namely the gradient Richardson’s Number.

3.4.3 Gradient Richardson's Number

Gradient Richardson's Number, Ri, can be explained as a parameter expressing the relative magnitude of buoyancy and mechanical forces, which can be expressed as the relative importance of free versus forced convection (equation 6.5).

Ri is a dimensionless number. A positive number implies a stable atmosphere with laminar flow of air, and little or no turbulence, whereas an unstable atmosphere is represented by negative Ri, indicating a higher degree of turbulence. When Ri approaches 0 the temperature gradient coincides with the dry adiabatic lapse rate, and the condition of the atmosphere is considered neutral (Kaimal and Finnigan, 1994).
The flow in the atmosphere is said to alternate from laminar flow to turbulent flow at the point where Ri is less than R_C, Critical Richardson Number (Stull, 1988). The termination of turbulence is indicated by another value, R_T, so that the turbulence ceases when Ri becomes greater than R_T. The actual values of these two borders is still under debate, but it appears that $R_C = 0.21$ to $=0.25$ and
$R_T = 1.0$ (Stull, (1988); Kaimal and Finnigan (1994)).

The disadvantage of Richardson's Number seems to be that it does not relate to height, and therefore it does not give a complete description of the stability regime in the surface layer.
Frank and Kocurek (1994) have studied the atmospheric effect on velocity profiles, and they conclude that stable conditions reveal high z_0 values, while unstable conditions reveal low z_0 values, given the same wind speed. Equally, the computed u_* values will be higher in stable conditions than in unstable conditions for any given wind. The reduced values of u_* can be explained by the vertical mixing, driven by thermal convection, which leads to a vertical exchange of momentum. The mixing increases this wind speed in the lower portion of the profile, whereas, at the same time, the wind speed decreases higher up. The result is a velocity profile that changes little with height, and hence gives a low u_*. During periods of stable stratification, vertical exchange of momentum is low, due to a decrease in vertical mixing. This results in the air flow becoming stratified, in such a manner, that high wind speeds are vertically adjacent to lower wind speeds, producing a higher value of u_*.

3.5 SENSIBLE HEAT FLUX AND AIR TEMPERATURE

The vertical flow of sensible heat above a crop stand varies throughout the day. It is this flux of energy, sensible heat, which determines air temperature. The diurnal variations in temperature gradient, and hence stability, are due to changes in the surface radiation budget. At night, when the surface cools gradually due to long-wave emission, producing a ground-based radiation inversion, a negative sensible heat flux is generated. As soon as the sun rises the radiation budget becomes positive, and the surface temperature rises, generating an upward sensible heat flux (Oke, 1987).

Looking at the temperature profile above a smooth surface, such as short grass, there is a general diurnal pattern, following the fluxes of sensible heat. During a night with clear skies, a nocturnal temperature inversion is usually developed, with air temperature increasing with height. Just after sunrise the ground is heated and the air temperature just above the ground rises successively to create, first, an isothermal profile, and then a neutral temperature profile, which will gradually become unstable as the day proceeds. In the afternoon the air close to the ground reaches its highest temperature. As the sun sets the air temperature near the ground decreases, and soon the air temperature further up starts to decrease as well. The profile progressively develops a stable atmosphere again.

3.6 LATENT HEAT FLUX AND ATMOSPHERIC HUMIDITY

Just like the sensible heat flux governs the temperature in the lowest layers, the exchange of moisture between the surface and the atmosphere controls the humidity. The flux of latent heat mainly goes in the direction of evaporation. During daytime, evaporation might be high, but at night it is reduced, and in some cases reversed, producing dew (Oke, 1987).

In this study data of relative humidity was used at a preliminary stage to estimate the latent heat flux. Relative humidity describes the amount of water vapour in the air in relation to the maximum amount of water vapour the air can hold at that temperature. The diurnal cycle of humidity usually follows the reversed temperature curve (figure 3.3).

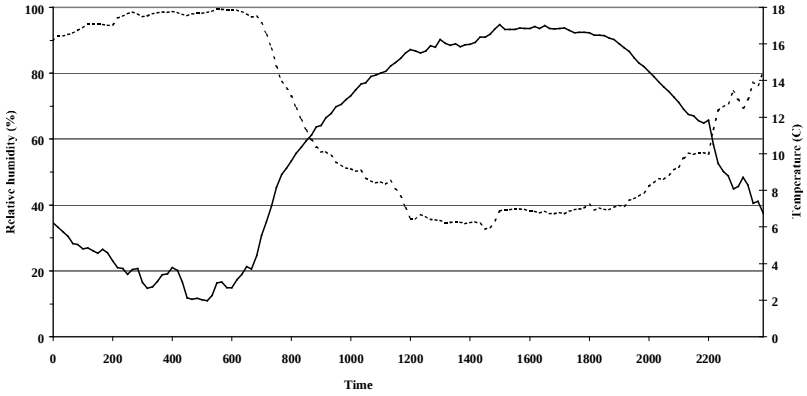

Figure 3.3 The diurnal cycle of relative humidity, dashed line, in relation to air temperature, solid line, at the same measurement height, Ilstorp, 1998.

At night relative humidity in the air is high, but when the sun comes up, and starts warming the surface, and the air, the relative humidity decreases. One reason to the decrease is that with increasing solar radiation, the temperature of the air increases, and hence can hold more water vapour than cold air. Also, the increased energy input is used for evaporation, which in turn generates an increase in latent heat flux up into the air.
This is clearly visible the study at Rothamsted, England (Oke, 1987), where the energy budget above a field of barley has been calculated (figure 3.4). During the day latent heat flux was high showing that most of the radiation was used for evaporation, which lead to little energy left to heat the crop and the air, and hence a low sensible heat flux.

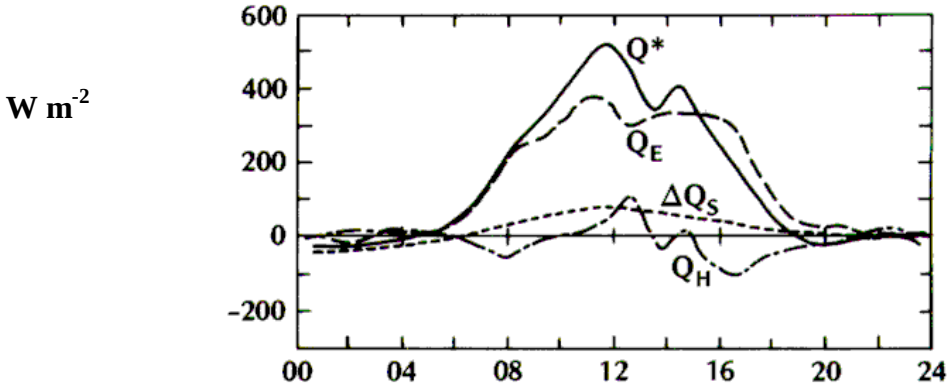

Figure 3.4 The energy budget above a field of barley, Rothamsted, England, 23th of July 1963, showing net radiation, Q, sensible heat flux, Q_H, latent heat flux, Q_E, and soil heat flux, ΔQ_s. Reference: Oke, 1987. figure 4.15 (b), p 135, modified after Long, I.F, Monteith, J. L., Penman, H.L. and Szeicz, G., 1964, The plant and its environment, Meteorol. Rundsch., 17: 97 – 101.*

3.7 SOIL HEAT FLUX AND SOIL TEMPERATURE

The two factors determining the rate of soil heat flux are the soil temperature gradient and the thermal conductivity. The soil temperature gradient, dT/dz, shows how temperature changes with soil depth and it is often exemplified by a temperature profile. Heat will continually move in and out of the soil, and this leads to thermal energy being constantly redistributed within the soil. Only during the isothermal conditions (no temperature gradient present) will heat not flow.

A typical diurnal soil temperature profile is shown in figure 3.5 (Rosenberg *et al.*, 1983). The figure shows that the largest diurnal temperature variations occur near the earth's surface, to a depth of 50 cm. Below 50 cm, variations in temperature gradient mainly depends on the seasonal temperature changes.
Concentrating on the variations in temperature within the first half meter the temperature profiles show that in the early morning the minimum temperature is found at a depth just below the earth. As the day proceeds sunlight heats the soil surface, and heat is progressively transferred down into the soil. It will take the heat some time to penetrate down, which is shown in the graph by the increasing time lag with depth. Hence, while the maximum temperature at the soil surface is reached in the early afternoon, the maximum temperature at a soil depth of 20 cm is not reached until late afternoon/early evening. By that time the temperature at the surface has sunken due to the decrease in sunlight. Heat is now being transferred from the soil depth of 20 cm both downwards into lower depths as well as towards the surface.

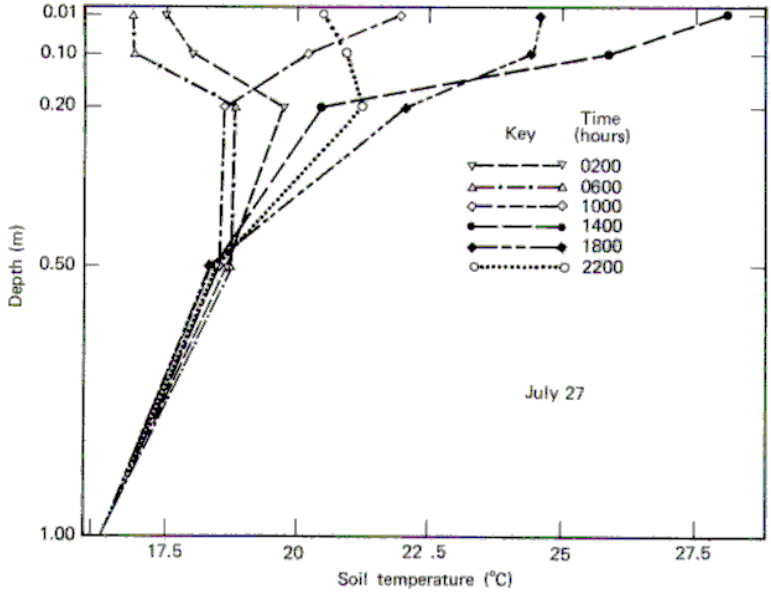

Figure 3.5. Temperature profiles in soil during a normal summer day at Argonne, Illinois. Reference: Rosenberg, N. J., Blad, B. L. and Verma, S. B., 1983, "Microclimate – The biological environment", Second edition, John Wiley & Sons, New York, p. 101, figure 2.3 after a study by Carson and Moses, 1963.

The second parameter influencing the rate of soil heat flux, the bulk thermal conductivity, is a measure of the capability to conduct heat. It depends on soil properties such as porosity, moisture content and organic matter content. In general thermal conductivity decreases with particle size and increases with moisture content. The thermal conductivity in sandy soil with 40% pore space range from 0.30 $Wm^{-1}K^{-1}$ for dry soil to 2.20 $Wm^{-1}K^{-1}$ for saturated soil (Oke, 1987).

The annual soil temperature variation follows a wavelike pattern similar to the diurnal cycle. The daily pattern might influence the top 0.75 m in the ground, but the annual cycle may have an effect down to depths of 14 m. In general, the soil temperature decreases with depth during the warm season, and a heat store is built up in the ground. As it becomes colder in the autumn

the store is gradually depleted by an upward soil heat flux, which persists during the winter. In springtime the temperature gradient is reversed again, and a new transfer of heat downward begins.

The relation between soil heat flux (Q_G), temperature gradient (dT/dz) and thermal conductivity (k_s) can be expressed as Fourier´s law (Oke, 1987):

$$Q_G = -k_s \frac{d\overline{T_s}}{dz} = -k_s \frac{\left(\overline{T}_2 - \overline{T}_1\right)}{\left(z_2 - z_1\right)} \tag{3.10}$$

The diurnal variation of soil heat flux shows a wavelike pattern, with a peak just after midday and a minimum just after midnight. The heat flux in the topsoil usually ranges between 0 – 20 W m^{-2} during a summer day.

4. FIELD SITE

The study site was located in Ilstorp, south west of Sjöbo, in Skåne. The levelled heights around Ilstorp, rise 4 – 8 m above the Vomb plain, at about 40 m above sea level, and slope slightly towards the south. An instrumented 10 m mast was positioned in between two fields ca 500 m from Ilstorpgården at co-ordinates 1365 560, 6166 660 (the Swedish co-ordinate system RT-90). Two separate masts were placed in each of the two adjacent fields, figure 4.1.

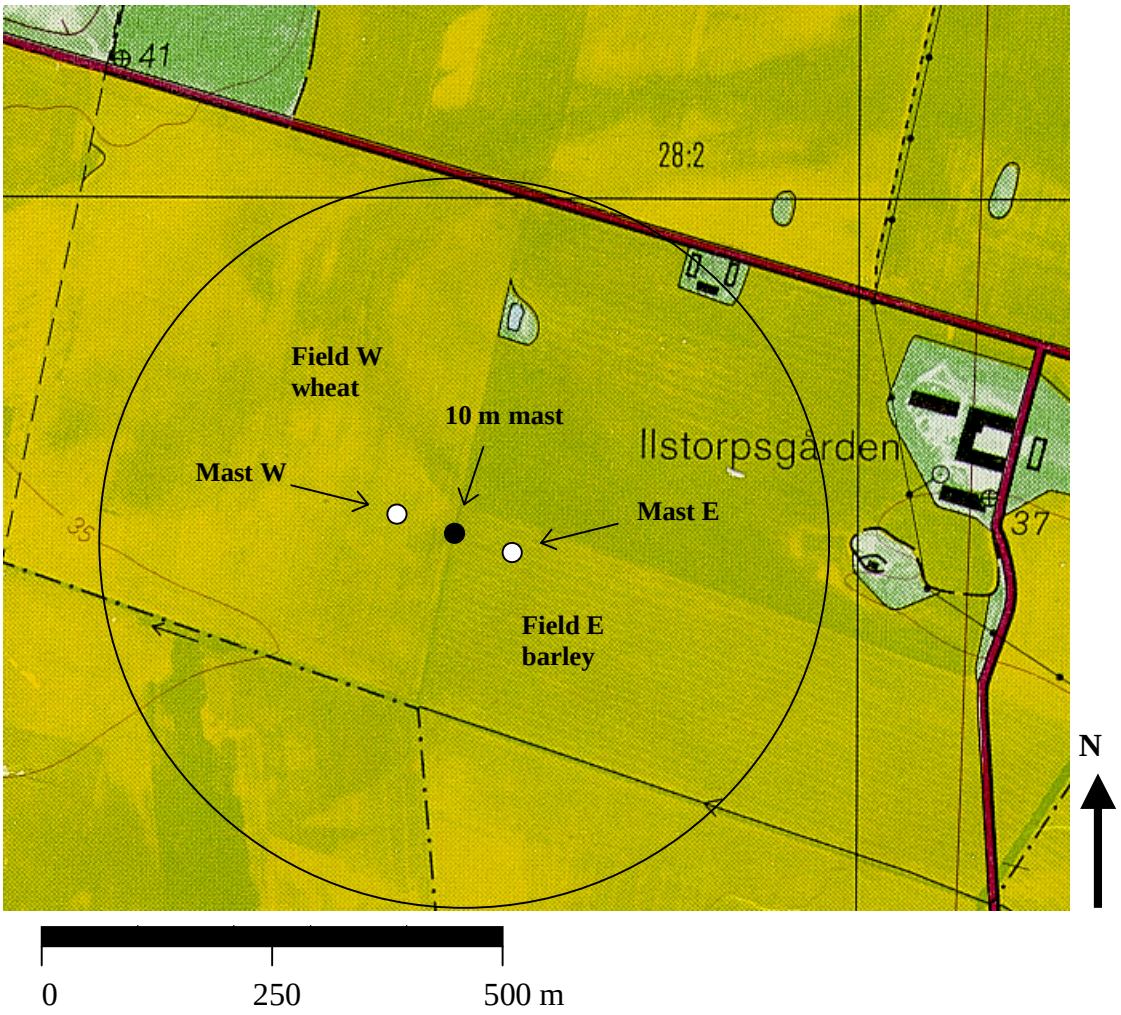

Figure 4.1 Map showing the site at Ilstorp, with the 10 m mast, Mast W and Mast E marked. Clear fetch by a radius of 400 m is shown.

4.1 TOPOGRAPHY AND SOIL

The Ilstorp region constitutes a part of the Vomb plain, which extends from Sjöbo to Vomb. The Vomb plain is a flat area, consisting mainly of glaciofluvial deposits and glaciolacustrine sediments, which are characterised by well sorted particles, transported and deposited by the melt water from the land ice cap during the last quaternary ice age (Daniel, 1992). The Vomb plain surface comprises primarily of sand and gravel with stones distributed locally. A large part of the glaciofluvial sediments is covered with fine sand, which easily become subject to wind erosion (Åhman, 1974).

4.2 LAND USE

The Ilstorp region is mainly used for cultivation of agricultural crops, such as wheat, barley, oats, sugar beets and potatoes. Several fields have had problems with strong wind erosion primarily during spring, and at some places stands of fast growing willow have been planted in shelterbelts.
The instrumented 10 m mast was located on the border between two fields. The western field, field W, was sown the previous autumn with wheat. The barley in field E, to the east of the mast, was sown in early spring. Both fields were harvested in the last week of August.

4.3 FETCH

The 10 m mast was situated 400 m from the main road, with a fetch northward extending above cultivated fields to at least 600 m north of the road. To the east the closest obstacle was the Ilstorp farm at a 500 m distance. A one meter narrow ditch at 160 m from the mast defined the southern borders of field W and field E. On the other side of the ditch further fields were found (figure 4.2). To the west Field W extended 500 m.

Just at the western border of field W a 5 m high sand dune, with aeolian sand, was located. On the opposite side of the road at the northern corner of field W a 5 hectare planted forest with predominantly conifers was established. The trees were estimated to be around 10 m high, and even though the closest tree was at a distance of near 500 m, care should be taken to wind direction data from the north-west. In conclusion the mast had a totally clear fetch by a radius of around 500 m.

The fetch recommended for a fully adjusted boundary layer is said to be 100 – 300 m fetch per each 1 m in vertical (Oke, 1987). In this study the fetch is sufficient in all weather directions up to measurements at 5 m. The data used from 10 m height might be disturbed when wind directions come from NW.

Figure 4.2 View towards the south looking over the springsown barley in field E. One of the short masts is seen in the field to the left. The lower part of the 10 m mast is seen to the right. The farm is about 600 m away. Ilstorp 98 04 29.

5. FIELD MEASUREMENTS

5.1 INSTRUMENTS AND SENSORS

Data for the study was obtained by sensors mounted on three instrumented masts; a 10 m mast (M10) and two 2 m masts (mast W and E). The 10 m mast (figure 5.1) held instruments measuring wind speed, wind direction, air temperature and air humidity (table 5.1). The 2 m masts (figure 5.1) carried thermocouples for temperature measurements in the air and in the soil. The site also included measurements of incoming short wave radiation, precipitation and soil heat flux (figure 5.1 and table 5.1).

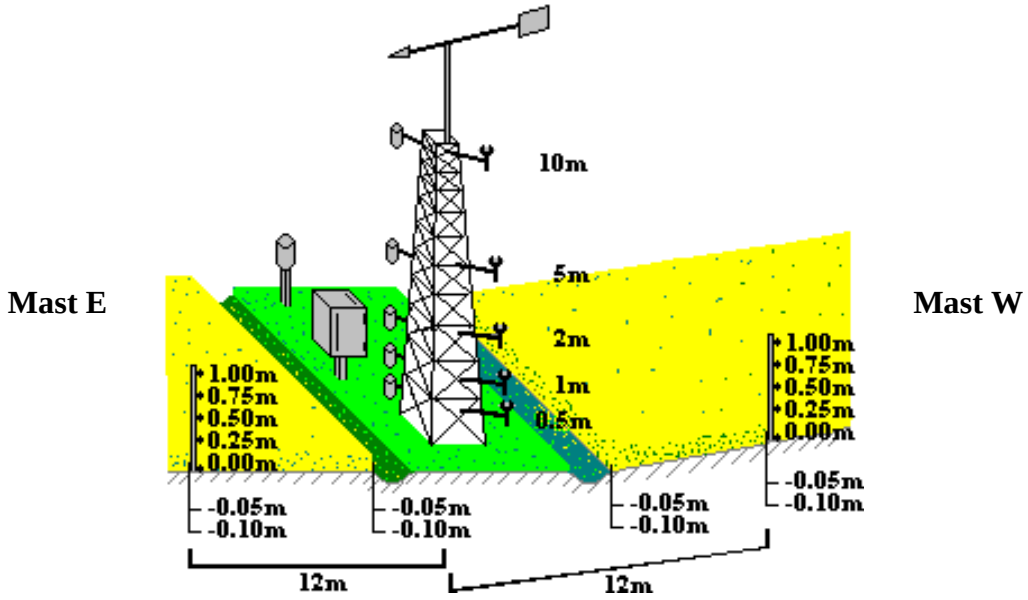

Figure 5.1. Study site with masts and instruments, Ilstorp, Sjöbo. View towards southwest.

Table 5.1 Instruments at the Ilstorp site. M10 refers to the 10 m mast. Mast E and mast W refer to the masts in the fields of barley and wheat respectively.

Instruments	Manufacturer, Type	Position	Level
Wind vane	RM Young, Gill Microvane 12002	M10	10 m
Anemometer	RM Young, Gill 3-cup 12102	M10	10 m, 5 m, 2 m, 1 m, 0.5 m
Humidity probes	Rotronic, MP100A	M10	10 m, 5 m, 2 m
Thermocouples	Pentronic, 0.51 mm	M10 Mast E and W	10 m, 5 m, 2 m, 1 m, 0.5 m 1 m, 0.75 m, 0.50 m, 0.25 m, 0 m, - 0.05, - 0.10 m
Heat flow sensors	RdF Corporation, 27025	at border of field E and W	- 0.05 m, - 0.10 m
Rain gauge	C-E Larsson AB, no 34	5 m south of 10 m mast	
Pyranometer	Kipp & Zonen, CM6B	3 m south of 10 m mast	

Data was collected by two Campbell dataloggers, CR10, both expanded with a multiplexor, AM32 (Campbell Scientific Ltd., Leicestershire, UK). The sensors were scanned with a 10 s interval and 10 minutes averages were calculated (datalogger program in Appendix A1) and stored in storage modules, SM192/SM716 and CSM1 (Campbell Scientific Ltd., Leicestershire, UK). The dataseries started on the 29th of April 1998, and continued until the 14th of September

1998. Data was processed and analysed with PC208w Datalogger Support Software (1997), Microsoft Access 97, Microsoft Excel 97, Pgraph version 1.0 (1989) and Minitab version 11.12 (1996).

5.1.1 Temperature measurements

Air and soil temperatures were measured using thermocouples (Pentronic P-24-T copper-constantan cable) with a diameter of 0.51 mm. The sensing junction was made by twisting and soldering the wires of copper and constantan threads together in a loop. The loop shape enabled a faster response time for the sensor (Blennow, 1997).

The thermocouples measured temperatures at heights of 1 m, 0.75 m, 0.50 m, 0.25 m and 0 m along two masts in field W and E respectively (Table 5.1) (Bärring *et al.*, 1999). Measurements were also made at the depth of 0.05 m and 0.10 m in the ground. The sensors in the ground had been attached to two bamboo sticks, which were inserted into the ground next to the two masts. On the 10 m mast thermocouples were mounted at 10 m, 5 m, 2 m, 1 m and 0.5 m.

The spacing of the thermocouples on the small masts were made with respect to the growth of the crop. Since the zero plane level is successively displaced as crop height increases, an even spacing was favoured. On the 10 m mast the instruments were mounted logarithmically while it is known that the properties change rapidly with height at near surface level (Oke, 1987).

The sensors on mast E and W were protected from direct solar radiation by aluminium tubes (diameter 5 cm, length 12 cm), that were painted black inside. The metallic outside of the tubes was mounted in a north-south direction to minimise the possibility of short wave radiation seeking its way in and heating the sensors. On the 10 m mast the thermocouples were inserted in radiation shields (Campbell Scientific Ltd., Leicestershire, UK) designed for both humidity and temperature sensors (Bärring *et al*, 1999).

The thermocouples were calibrated in ice slush and at room temperature prior to field measurements. The datalogger program for calibration of thermocouples is found in Appendix A2.

5.1.2 Heat flow measurements

Heat flow in the ground was measured at two levels at the border of each field, using four Mirco-foil Heat Flow Sensors model 27025 (RdF Corporation, Hudson, New Hampshire). With these sensors the heat flux can be measured directly, without taking soil thermal properties into account. The sensors consist of thin plates with known heat conductivity. They are placed in the soil and the temperature gradient over the plates, measured by thermopiles, is proportional to the current heat flow in the soil (Loman, 1986).

The heat flow sensors were placed at depths of 0.05 m and 0.10 m in each of the fields (table 5.1). Preferably these sensors should have been placed near the temperature sensors, but due to cultivation of the fields the heat flow sensors had to be located at the border of each field (figure 5.1) A multiplicator of 500 was used to convert the voltage reading of the sensors into Wm^{-2}.

5.1.3 Wind speed and wind direction

Wind speed was recorded with five Gill three-cup anemometers, model 12102 (R.M Young Company, Michigan, USA). The instruments were mounted at 10 m, 5 m, 2 m, 1 m and 0.5 m on the 10 m mast (figure 5.1). All anemometers were placed 1 m out from the mast on booms pointing towards north. The Gill three-cup anemometers have a threshold wind speed of 0.35 - 0.45 m s^{-1}, which is caused by the friction of the bearings and generator assembly.

Prior to the field study the anemometers had been calibrated in the wind tunnel at the Department of Animal Ecology, Lund. The anemometers were tested at wind speeds of 12 m s^{-1} and 3.6 m s^{-1}, with a scanning interval of 1 s during 10 minutes (Bärring *et al*, 1999). The individual mean wind speed was calculated, and each anemometer reading was corrected using the anemometer at 10 m as a reference. The corrections ranged from -0.013 m s^{-1} to 0.017 m s^{-1}.

Wind direction was obtained with Gill Microvane, model 12002 (R.M Young Company, Michigan, USA) mounted on the 10 m mast (Bärring *et al*, 1999).

5.1.4 Air humidity

Air humidity was measured at 10 m, 5 m and 2 m with three Hygromer meteorology probes MP100A (Rotronic, Messgeräte Gmbh, Ettlingen). The instruments contained both an air humidity sensor - Rotronic-hygromer C94, and a temperature sensor - RTD Pt100 1/3 DIN. The instruments were calibrated as indicated in the Operating Instructions, at relative humidity of 35 % and 95 % (solutions of LiCl) (Bärring *et al*, 1999). It was found that at high relative humidity the three sensors were within an accuracy of 1 %, but at low relative humidity one of the sensors showed a 5 % higher measurement. The accuracy of the temperature sensors was 0.3 °C.

The humidity probes were placed inside radiation shields (Campbell Scientific Ltd., Leicestershire, UK), constructed so that no rain or water could come in direct contact with the sensors.

5.1.5 Precipitation

A tipping bucket rain gauge (No 34, Ingenjörsfirma Carl-Eric Larsson AB, Stockholm) was used to register rainfall (Bärring *et al*, 1999). The rain water is collected by a funnel and led down to one of two buckets. When the first bucket contains 0.5 mm water it tilts over and triggers a relay. At the same time the second bucket is positioned under the funnel to collect the next 0.5 mm before it tilts, and the procedure is repeated as long as the rain falls. When the relay is triggered it connects a circuit during 0.13 s, and a pulse is sent to the datalogger.
The rain gauge was protected by a cylinder, with a height of 47 cm and a diameter of 20 cm. The instrument was carefully adjusted, ensuring the buckets to contain 0.5 mm precisely.

5.1.6 Irradiance

Incoming direct solar radiation and diffuse radiation incident from the hemisphere above was measured with a pyranometer, model CM6B (Kipp & Zonen Delft). The pyranometer had a spectral range from 335 nm to 2,200 nm, and it was placed on top of the logger cupboard 3 m south of the 10 m mast (Bärring *et al*, 1999).

The sensing element of the pyranometer consists of a thermopile with black and white segments. The irradiance is absorbed by the black segments and reflected by the white ones, and so the temperature difference between the segments can be measured and converted into a voltage measurement (Rosenberg *et al*, 1983). A double glass dome protects the thermopile from cooling by wind and rain.

5.2 FIELD WORK ROUTINES

The field study area was inspected on a weekly basis, and data in the storage modules was collected. The instruments were checked and the batteries were replaced if necessary. During the summer a solar panel was installed at the climate station, charging the Campbell logger battery to the 10 m mast with solar power. The crop height of the wheat and the barley in field W and E was noted at each field visit.

This page is left blank intentionally!

6. METHODS

This chapter will describe the methods and steps used to obtain estimates of the energy budget components. It starts with explaining the general theory of gradient-profile methods, and the calculations of atmospheric stability. Then, the foundation of these equations, the logarithmic wind profile together with the temperature profile, will be discussed, and the equations for estimating zero plane displacement height, roughness length and friction velocity are presented. Finally, the separate calculations of sensible and latent heat, as well as net radiation, are dealt with.

6.1 GRADIENT-PROFILE METHODS

Gradient-profile methods are based on the principle of similarity regarding the diffusion of momentum, sensible heat, latent heat and carbon dioxide. It states that the diffusion coefficients for the flows of momentum (K_M), heat (K_H), water vapour (K_V) and carbon dioxide (K_C) are equivalent in neutral stability.

$$K_M = K_H = K_V = K_C \tag{6.1}$$

This means that an eddy will just as easily carry momentum, heat, water vapour or carbon dioxide (Oke, 1987). The principle of similarity allows the fluxes of momentum, sensible heat and latent heat to be estimated by analogous equations (Oke, 1987);

$$\tau = \rho k^2 \left[\frac{\Delta u}{\ln(z_2 / z_1)} \right]^2 \quad \text{momentum flux} \tag{6.2}$$

$$Q_H = -C_a k^2 \frac{\Delta u \Delta T}{\left[\ln(z_2 / z_1)\right]^2} \quad \text{sensible heat flux} \tag{6.3}$$

$$Q_E = -L_v k^2 \frac{\Delta u \Delta \rho_v}{\left[\ln(z_2 / z_1)\right]^2} \quad \text{latent heat flux} \tag{6.4}$$

ρ represents the air density and ρ_v is the mean absolute humidity (g m^{-3}), k is von Karman's constant at 0.40, C_a stands for the heat capacity of air (J m^{-3} K^{-1}), and L_v is the latent heat of vapourization (J kg^{-1}). The mean wind speed, u (m s^{-1}), and mean temperature T (K) are used from the measurement height z_1 and z_2 (m).

These equations are, however, only valid when buoyancy effects are absent, indicating neutral stability. Furthermore, the observation period should show no sign of abrupt changes in the radiation or wind fields, and there should be a constancy of fluxes with height (Oke, 1987).
To distinguish the neutral atmospheric conditions from the stable and unstable conditions the gradient Richardson's Number was used.

6.2 ATMOSPHERIC STABILITY

Atmospheric stability was calculated by using the formula for gradient Richardson's Number, Ri.

$$Ri = \frac{g}{\overline{T}} \frac{(\partial\theta / \partial z)}{(\partial u / \partial z)^2} \tag{6.5}$$

where T is the average temperature in the layer $z_2 - z_1$ expressed as Kelvin. The value of 9.82 m s^{-2} was used as gravity, g. Differences in wind speed, ∂u, and potential temperature, $\partial\theta$, was calculated using data from 10 m and 2 m (z_2 and z_1).

Potential temperature was obtained with equation;

$$\theta = T - \Gamma z \tag{6.6}$$

where Γ is the dry adiabatic lapse rate of approximately 0.01K m^{-1}.

Richardson's Number was then used to divide data into three categories of atmospheric stability. With Ri greater than 0.01 the stability condition was said to be stable, whereas instability was represented by Ri below – 0.01. Neutral atmospheric conditions ruled when
– 0.01 < Ri < 0.01 (Oke, 1987).

According to Frank and Kocurek (1994) Ri can also be used in defining the degree of convection in the atmosphere (Table 6.1).

Table 6.1. The relation between Gradient Richardson's Number and convection.
Source: Frank, A., and Kocurek, G., 1994, Effects of atmospheric conditions on wind profiles and aeolian sand transport with example from White Sands National Monument, Earth surface processes and landforms, 19: 735 – 745

Ri < - 1.0	Free convection
- 1.0 < Ri < - 0.01	Mixed convection
- 0.01< Ri < 0.01	Fully forced convection
0.01 < Ri < 0.2	Damped forced convection
Ri ≥ 0.2	No convection

6.3 PROFILES OF WIND SPEED AND TEMPERATURE

Temperature and wind speed measurements were plotted against height as profiles for various periods during the growing season, in order to evaluate how the wind and temperature regimes were effected by the increasing crop height. The wind speed data were selected on the basis of neutral stability (-0.01 < Ri < 0.01) and wind direction, to get the appropriate fetch. Wind directions between 40° and 140° were used for wind profiles above field E, and above field W wind directions between 220° and 320° were selected.

6.3.1 Zero plane displacement height (d)

The zero plane displacement height d, was calculated using an equation constructed by Stanhill, 1969 (Rosenberg *et al.*, 1983), where *d* was estimated directly from the crop height, *h*.

$$\log_{10} d = 0.979 \log_{10} h - 0.154 \tag{6.7}$$

The value of *d* was also approximated by using the following equation from Oke (1987):

$$d = \frac{2}{3}h \tag{6.8}$$

Results from the two calculations were compared. The displacement heights estimated from Oke´s equation were in general lower than those from Stanhill´s equation. It was decided to use Stanhill´s equation, since it was based on empirical data (figure 7.10 (a) and (b)).

6.3.2 Roughness length z_0 and friction velocity u_*

Rosenberg *et al.* (1983) mentions that Szeicz *et al.*, 1969, has empirically related roughness length to crop height by the equation:

$$\log_{10} z_0 = 0.997 \log_{10} h - 0.883 \tag{6.9}$$

This equation was used to estimate the roughness length in comparison to the wind profile plotted against the logarithm of height. The result can be seen in figure 7.10 (a) and (b).
The roughness length was also determined from the logarithmic wind profiles, as the y-axis intercept of the elongated calculated regression line, table 7.1.
The slope of the calculated regression line (figure 3.2 (b)) were used to find the friction velocity, u_*, table 7.1.

6.4 FLUXES OF SENSIBLE AND LATENT HEAT

6.4.1 Correction factors

Since the gradient-profile equations (6.2 – 6.4) are only valid during neutral atmospheric conditions, there are a number of correction factors in the literature to compensate for unstable and stable atmospheric conditions. In this study the generalised stability factor F, introduced by Thom in 1975 (Oke, 1987, Monteith and Unsworth, 1990) has been used. The corrections for stable and unstable atmospheres using F are (Oke, 1987):

Stable atmosphere	F	=	$(1 - 5\mathrm{Ri})^2$
Unstable atmosphere	F	=	$(1 - 16\mathrm{Ri})^{3/4}$

6.4.2 Sensible and latent heat flux

Sensible heat flux was calculated using profile data of wind speed and temperature at 10 m and 2 m in equation (6.3). The value of 1200 J $m^{-3}K^{-1}$ was used as heat capacity of air, C_a (Oke, 1987).
After the sensible heat flux had been calculated, the latent heat flux was found as the residual term using the surface energy balance (eq. 3.6) in the modified version;

$$Q_E = Q^* - Q_H - Q_G \tag{6.10}$$

Q_H and Q_G were acquired from earlier calculations and field data respectively. Preferably net radiation, Q*, should have been measured directly by a net radiometer, but in this particular study such an instrument was not available. Instead net radiation was obtained by theoretical calculations in Pgraph. The input data included incoming short wave radiation from a pyranometer and ground surface temperature data from field W and E. Surface albedo was approximated from earlier studies (Oke, 1987). The calculations in Pgraph were based on latitude, albedo, air temperature and humidity, global radiation and cloudiness (table 6.2).

Table 6.2 Input variables for calculation of net radiation. For air temperature, air humidity and global radiation field data was used. Latitude was derived from a map, and different values of albedo were tried out. No data were available on amount of cloudiness. Hence, the net radiation calculations are only valid for sunny days.

Variable	Unit	Input value
Latitude	degrees	55°
Albedo	%	25 %
Air temperature	°C	Measured data
Air humidity	%	Measured data
Global radiation	J/m^2 day	Measured data
Cloudiness	Fraction/minute	No data

The equations for calculating net radiation in Pgraph are based on eq. (3.2 – 3.5).
Net radiation was calculated for the period of 11/5 to 29/6 using an albedo of 18 % and 25 % (suggested range for albedo above agricultural crops, Oke, 1987), in order to see how the global radiation calculations varied with albedo. Logically it was found that a lower albedo gave a higher net radiation. The difference in net radiation between calculations using an albedo of 18 % and 25 % ranged from 0 W m^{-2} in the early morning and late afternoon, to just above 70 W m^{-2} at midday. A general albedo of 23 % was chosen to be used during the entire study period.
No data was available on the amount of cloudiness, but the data on used for global radiation indirectly included variation in cloud cover.

6. 5 SELECTION OF DATA

In order to estimate the continuous change of microclimatological properties during the growing season four separate periods were chosen for detailed study (table 6.3). The periods were chosen on the basis of the amount of cloud free days, days when the short wave radiation had not been disturbed. Unfortunately the summer of 1998 was not famous for its sunny days, and this has led to a very narrow selection of possible days to be chosen. Temperature profiles are plotted for the same days as the energy balance estimations, but the wind profiles rely on times of neutral conditions, which explains the dates chosen.

Table 6.3. Selected dates in order to calculate energy fluxes, temperature profiles and logarithmic wind profiles.

Month	**Dates** ***Heat fluxes***	**Dates** ***Temperature***	**Dates** ***Wind Field W***	**Dates** ***Wind Field E***	**Crop height (cm) on dates of flux calculations (dates of wind profiles)**	
					Field W	**Field E**
MAY	16	16	21	28	60 (65)	15 (30)
JUNE	21	21	24	28	120 (120)	80 (95)
JULY	22	22	22	23	115 (115)	80 (80)
AUGUST	11	11	23	13	110 (100)	75 (70)

7. RESULTS

7.1 GENERAL WEATHER DISCRIPTION

7.1.1 Radiation

In figure 7.1 five-day short-wave radiation average and maximum are plotted for the whole measuring season, 980511 – 980914. Most days during early summer solar radiation reached a maximum value of 800 – 1000 Wm^{-2} during the afternoon. In early July solar radiation stretched to its peak value of 1152 Wm^{-2}. Thereafter, a gradual decrease in maximum solar radiation was noted. The average solar radiation included nighttime data, which obviously dragged down the mean value.

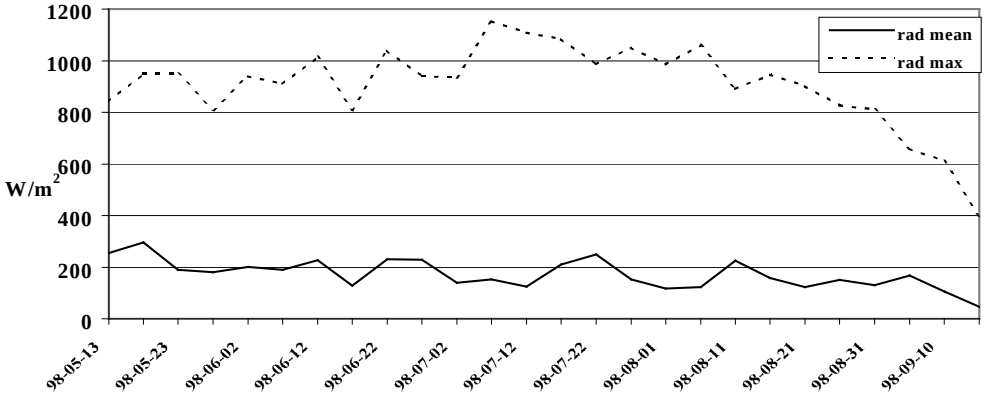

Figure 7.1 Five-day averages, solid line, and five-day maxima, dotted line, of solar radiation (Wm^{-2}), from 980511 – 980914, at the Ilstorp site. The low averages include nighttime data.

7.1.3 Wind speed

Variations in wind speed during the measuring season can be seen in figure 7.2, where five-day averages were plotted for each of the measuring heights; 10 m, 5 m, 2 m, 1m and 0.5 m.

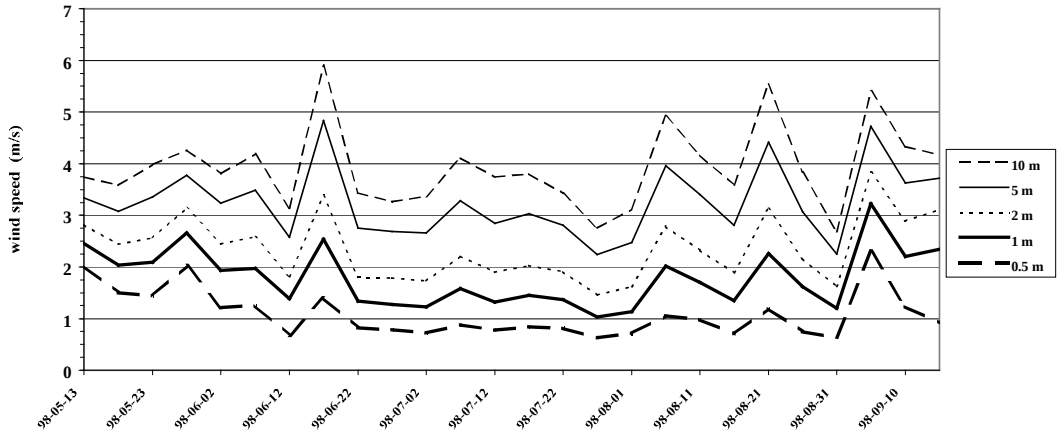

Figure 7.2. Five-day averages of wind speed (m/s) at heights of 10m, 5 m, 2 m, 1 m and 0.5 m from the 10 m mast in Ilstorp, 980511-980914.

In the beg
wind speed averages from 0.5 m to 10 m differed less than 2 m s^{-1}. As the crop grew the wind speed at the lower heights gradually decreased. At 0.5 m the five-day average seemed to stabilise around 0.6 – 1.0 m s^{-1} until the end of August, when the fields were harvested.

The maximum wind speeds at 10 m, figure 7.3, varied between 9 and 14 ms^{-1} during most of the measuring season, with the exception for two dips below 8 ms^{-1} in early July and in late August.

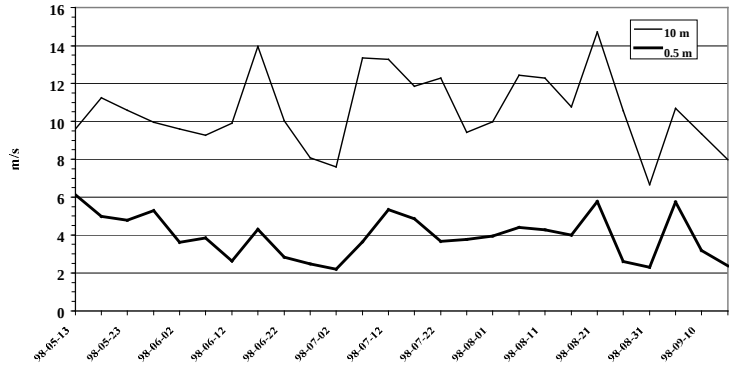

The maximum wind speed at 0.5 m showed a steady decrease from 6 ms^{-1} to near 2 m s^{-1} from May to early July. During mid-July to mid-August the maximum wind speed at 0.5 m has increased to just around 4 ms^{-1}.

Figure 7.3 Maximum wind speeds (m s^{-1}) at 10 m (thin line) and 0.5 m (thick line) for each five day period during the measuring season at Ilstorp, 98 05 11 – 98 09 14.

7.1.4 Temperature

The maximum and minimum ten-minute-average temperatures at 10 m and 0.5 m for intervals of five days are shown in figure 7.4. The maximum temperature curves at 10 m and 0.5 m followed each other closely. It is clear that the highest temperatures have been recorded closest to the ground. The average maximum temperature during the whole period was 19.8°C at 10 m compared 21.4°C at 0.5 m.

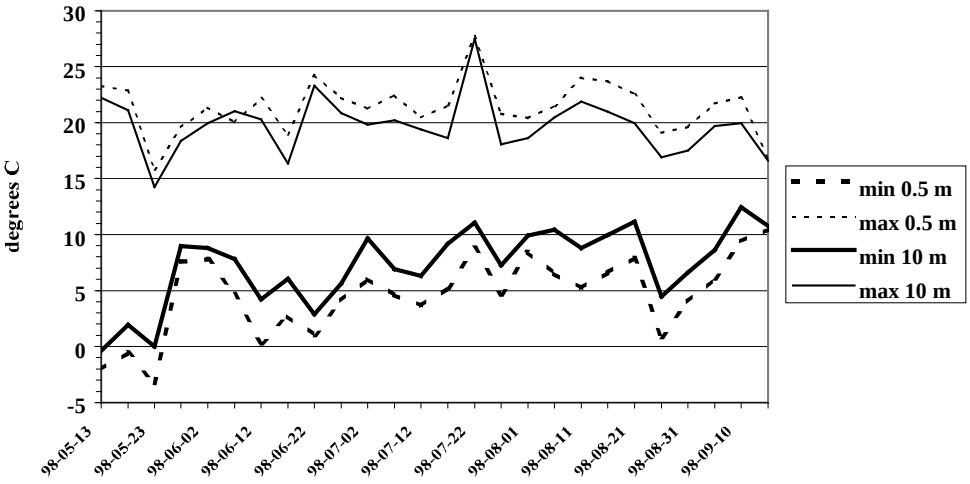

Figure 7.4 Minimum and maximum temperatures at 0.5 m (dashed lines) and 10 m (solid lines) for each five day period during the measuring season at Ilstorp , 98 05 11 – 98 09 14. The 10 m data derives from the PT100 sensor connected to the humidity probe, and the 0.5 m data originates from thermocouple measurements.

The minimum temperatures at 0.5 m indicated that night frost occurred until late May. After a quick increase in minimum temperature at both 0.5 m and 10 m there was a sudden fall at mid-June, where the temperature at 0.5 m dropped down to near 0°C again. The subsequent time period revealed a steady increase in minimum temperatures until the harvest in late August.

7.1.5 Wind direction

The wind direction during the whole measuring period is shown in figure 7.5. The prevailing winds were mainly westerly, and to some extent from the north. Easterly winds, which are usually stronger and more eager to start wind erosion, are not common after early spring.

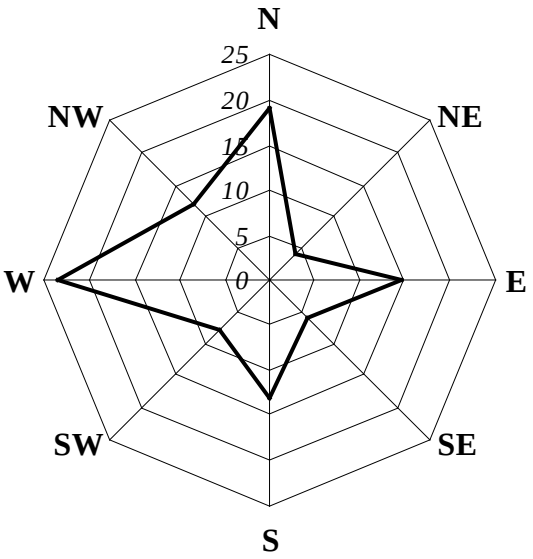

Figure 7.5 The relative frequency of the prevalent wind direction at Ilstorp, 98 05 11 – 98 09 14.

7.1.6 Humidity and precipitation

Relative humidity shows fluctuations between 75 % and 90 % during most of the growing season, figure 7.6, indicating a fairly wet summer. Monthly sums of precipitation were acquired from SMHI´s weather stations in Lövestad and Vomb, figure 7.7, since the rain gauge at Ilstorp malfunctioned during July and August.

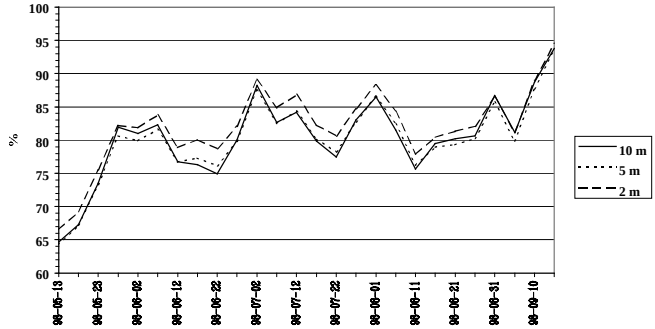

Figure 7.6 Five-day averages of relative humidity at 10 m (solid line), 5 m (dotted line) and 2 m (dashed line) at Ilstorp, 98 05 11 – 98 09 14.

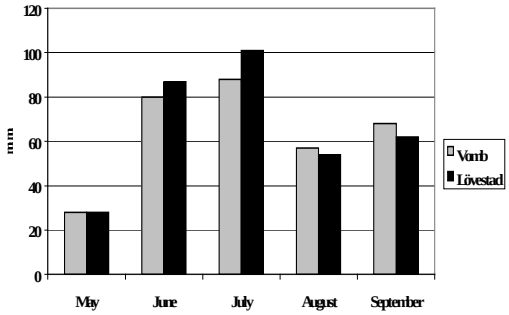

Figure 7.7 Monthly sums of precipitation Vomb and Lövestad. Data from Vomb and Lövestad were obtained from Haldo Vedin, SMHI, April 1999.

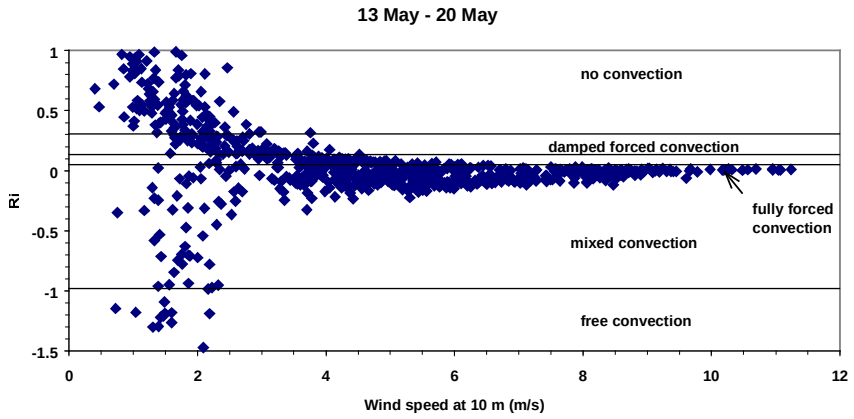

(a)

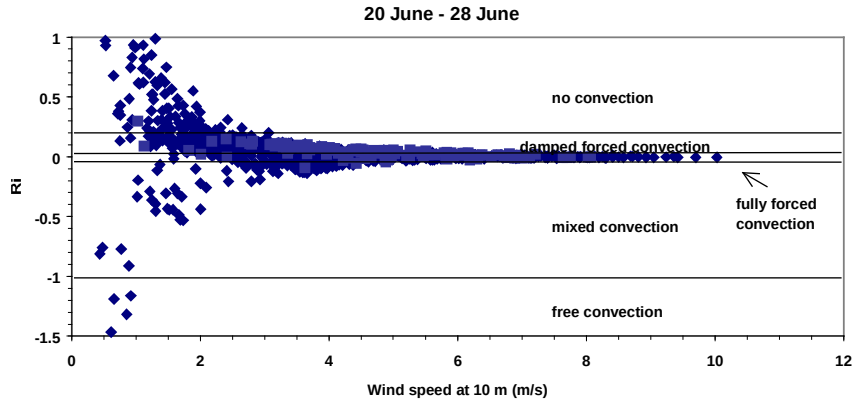

(b)

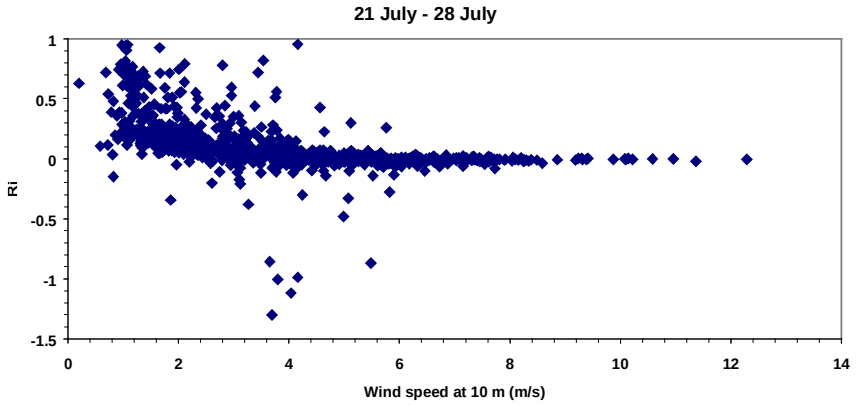

(c)

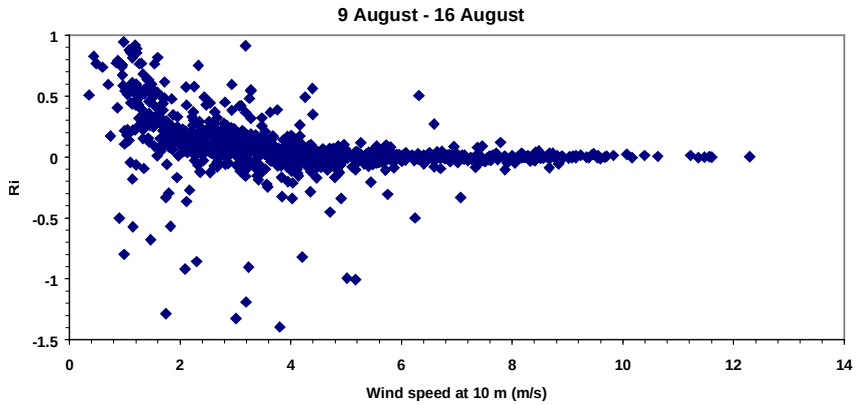

(d)

Figure 7.8 a – d. Plot of Richardsons number, Ri, versus wind speed at 10 m, during four time periods; (a) 13th – 20th of May, (b) 20th- 28th of June, (c) 21st – 28th of July, and (d) 9th – 16th of August, Ilstorp, 1998. Data are limited to fully forced convection (neutral) only above wind speeds of 4 m s^{-1} in (b), 6 m s^{-1} in (c) and (d). In (a) the border is more of a transition zone up to 8 m s^{-1}.

7.2 ATMOSPHERIC STABILITY

The atmospheric stability, estimated with gradient Richardson's Number (equation 6.5), was plotted against wind speed at 10 m height, figure 7.8 a – d (opposite page), at four periods during the measuring season. The figures show a wider range of Ri as the wind velocity decreased. Fully forced convection, with Ri between -0.01 and 0.01, occurred at high wind speeds. There seems to be a border at 4 m s^{-1} in figure 7.8 b, which is pushed forward to 6 m s^{-1} in figure 7.8 c and 7.8 d, after which fully forced convection was dominant. The occurrence of free convection at low wind speeds seems to change during the measuring season to take place at slightly higher wind speeds.

To find the diurnal pattern of atmospheric stability Ri was plotted versus the time of the day for the whole season, figure 7.9. At night conditions were always stable, but just after sunrise they became unstable. The unstable condition lasted during the day, and then returned to stable just before sunset.

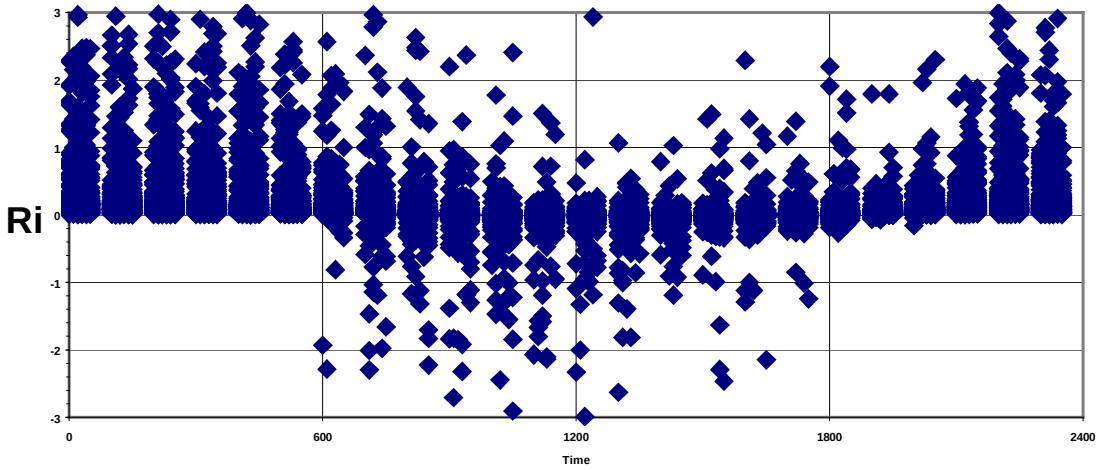

Figure 7.9. Diurnal variation of Richardsons number, Ri. During night-time conditions were stable, while neutral to unstable conditions dominated during the day. Data from the whole measuring period, Ilstorp, 1998.

7.3 THE LOGARITHMIC WIND PROFILE

7.3.1 Crop height, zero plane displacement height and roughness length

The zero plane displacement height was calculated using equation (6.7), and the roughness length was estimated with equation (6.8). In figure 7.10 (a) and (b) crop height in relation to calculated zero plane displacement height, d, and roughness length is shown.

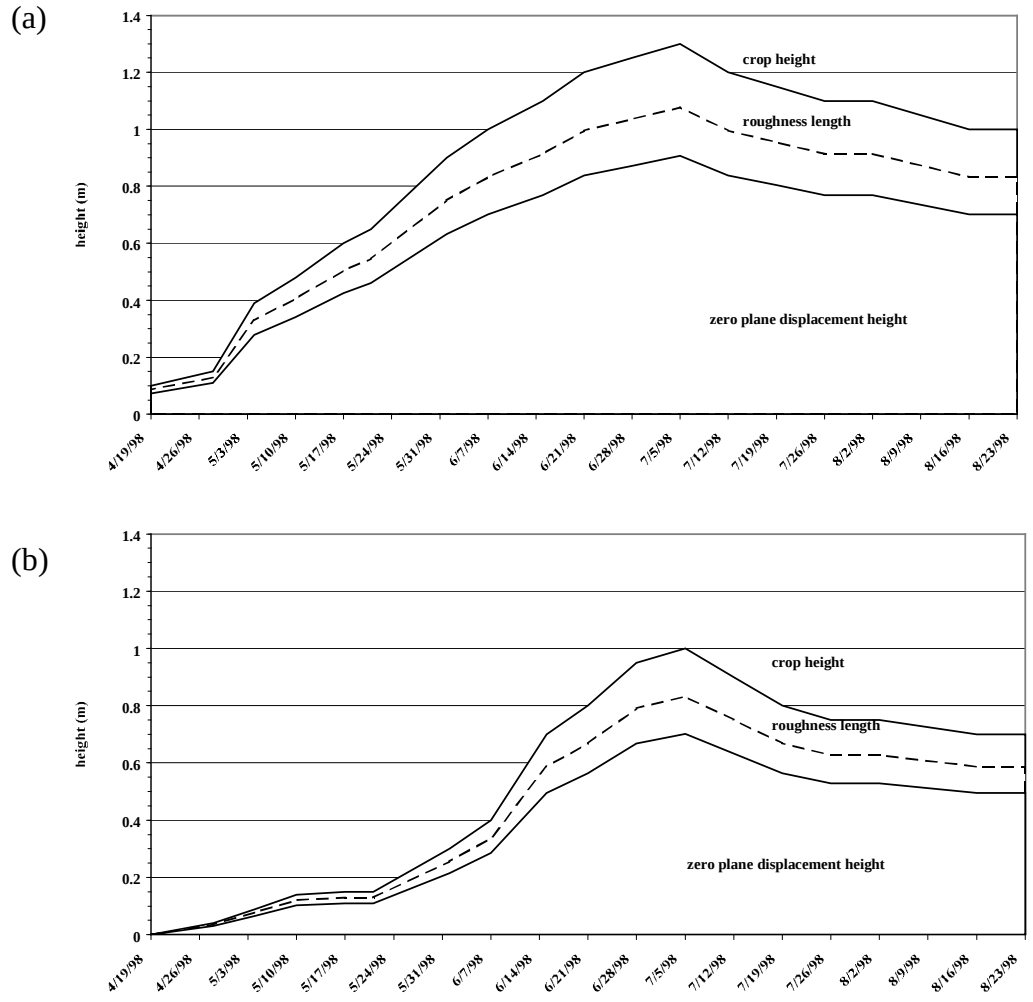

Figure 7.10 (a) and (b). Zero plane displacement height and roughness length in relation to crop height, during the measuring season in (a) field W and (b) field E, Ilstorp, 1998. Both the wheat and the barley were harvested in the last week of August. The decrease in actual crop height in the latter part of the summer was due to maturing of the crop, which effected the crop to gradually become bent as it dried. Note that the wheat was sown the previous autumn, which explains the generally higher crop stems in field W.

7.3.2 Wind profiles

For both fields wind profiles were plotted against the measurement height and the logarithmic height, figures 7.11 (a – h), and 7.12 (a – h). The selection criteria are outlined in Chapter 6.3 and table 6.3. Each line/profile in the graphs represents a time period of 10 minutes during that particular day.

Profiles are based on wind speed data from 10 m, 5 m, 2 m and 1m. The 0.5 m wind speed was omitted, since the crop in most cases were higher than 0.5 m. Figure 7.11 (a) however does include the 0.5 m wind speed. Logarithmic wind profiles include measurements of 10 m, 5 m, 2 m and 1 m.

7.3.3 Roughness length, friction velocity and transfer of momentum

For each date, in the graphs where wind speed was plotted against logarithmic height, the equation of the regression line was calculated (in Minitab). The regression line was then used to find the friction velocity, u_*, and the roughness length, d, with the logarithmic wind profile equation (equation 3.10). In table 7.1 the results are summarized. With an increase in crop height it is possible to note a distinct bend on the profiles plotted versus the logarithmic height (figure 7.11 (b – d) and 7.12 (b) and (d). In those cases the calculated regression line excluded wind speed measurements from 1 m. Table 7.1 also includes estimated transfer of momentum at the zero plane displacement height, given by equation (3.9).

Table 7.1. Data from the western field (wheat) and the eastern field (barley) showing crop height, zero plane displacement height, Y-axis intercept of calculated regression line, roughness length, slope of regression line and friction velocity and momentum transfer (equation 3.9).

Date	**crop**	**crop height** *(m)*	**displacement height** *(m)*	**y-intercept**	**roughness length** *(m)*	**slope**	**friction velocity** *(m/s)*	**momentum** *(N/m^2)*
21/5	wheat	0.65	0.460	-4.4666	0.011	0.7237	0.57	0.393
24/6	wheat	1.20	0.839	-2.4009	0.091	1.1026	0.37	0.169
22/7	wheat	1.15	0.804	-1.4350	0.238	0.4736	0.87	0.918
23/8	wheat	1.00	0.701	-2.2408	0.106	0.3682	1.11	1.519
28/5	barley	0.30	0.216	-4.0092	0.018	1.1735	0.35	0.150
28/6	barley	0.95	0.667	-3.2341	0.039	0.9521	0.43	0.227
23/7	barley	0.80	0.564	-1.5997	0.202	0.8573	0.48	0.280
13/8	barley	0.70	0.495	-1.4762	0.229	0.3972	1.03	1.305

7.4 TEMPERATURE PROFILES

Temperature profiles in and above the fields of wheat and barley were plotted for four different times during the growing season; 16th of May, 21st of June, 22nd of July and 11th of August, in figures 7.12 a-d and 7.13 a-d. Soil temperature measurements in figure 7.12 (a) and 7.13 (a) only include temperatures at the depth of 0.05 m.

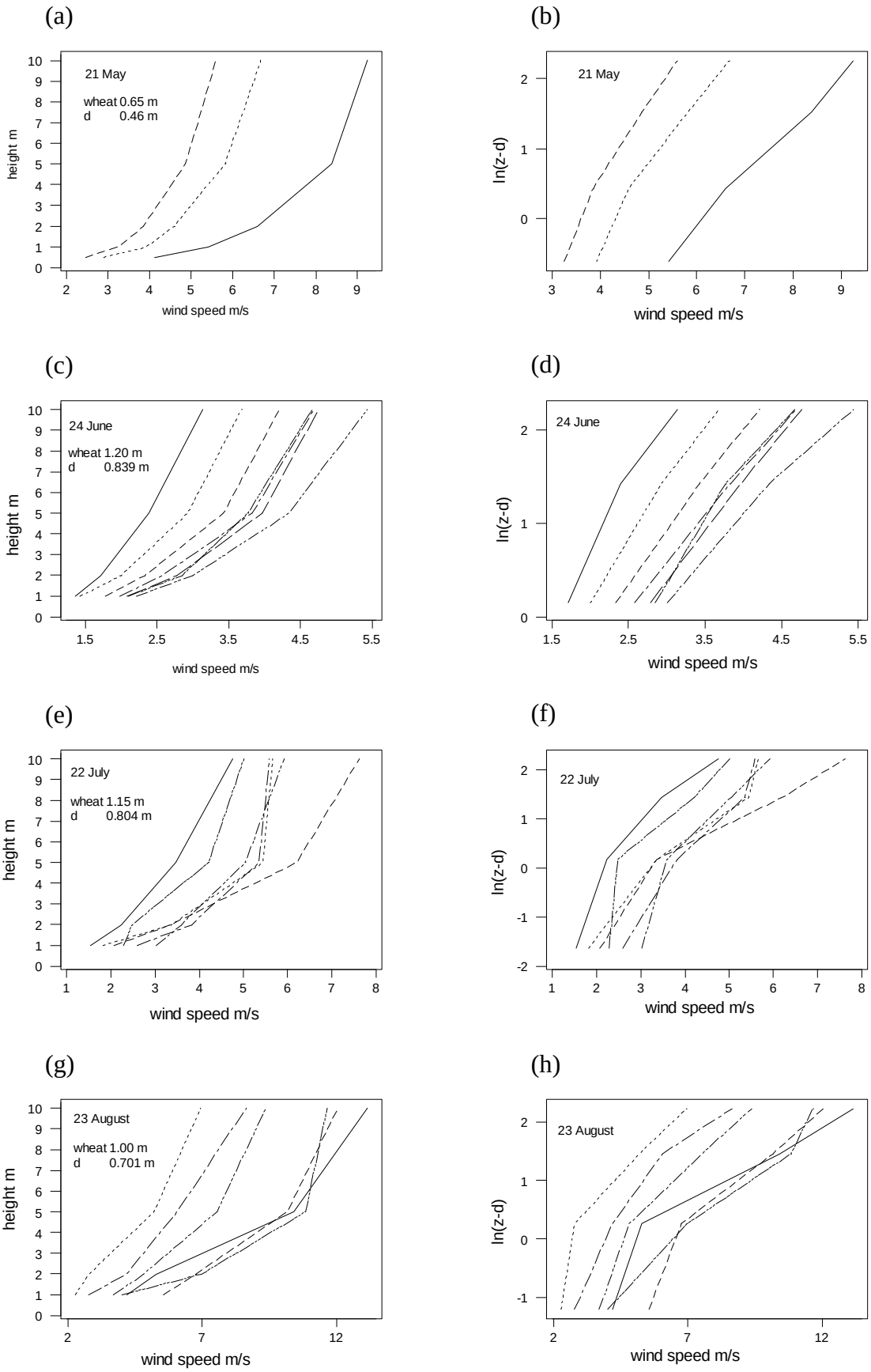

Figure 7.11 (a – h). Wind profiles representing winds above the western field, Ilstorp, plotted against height (z) and ln (z-d). Each profile in the graphs represent a time period of 10 minutes.

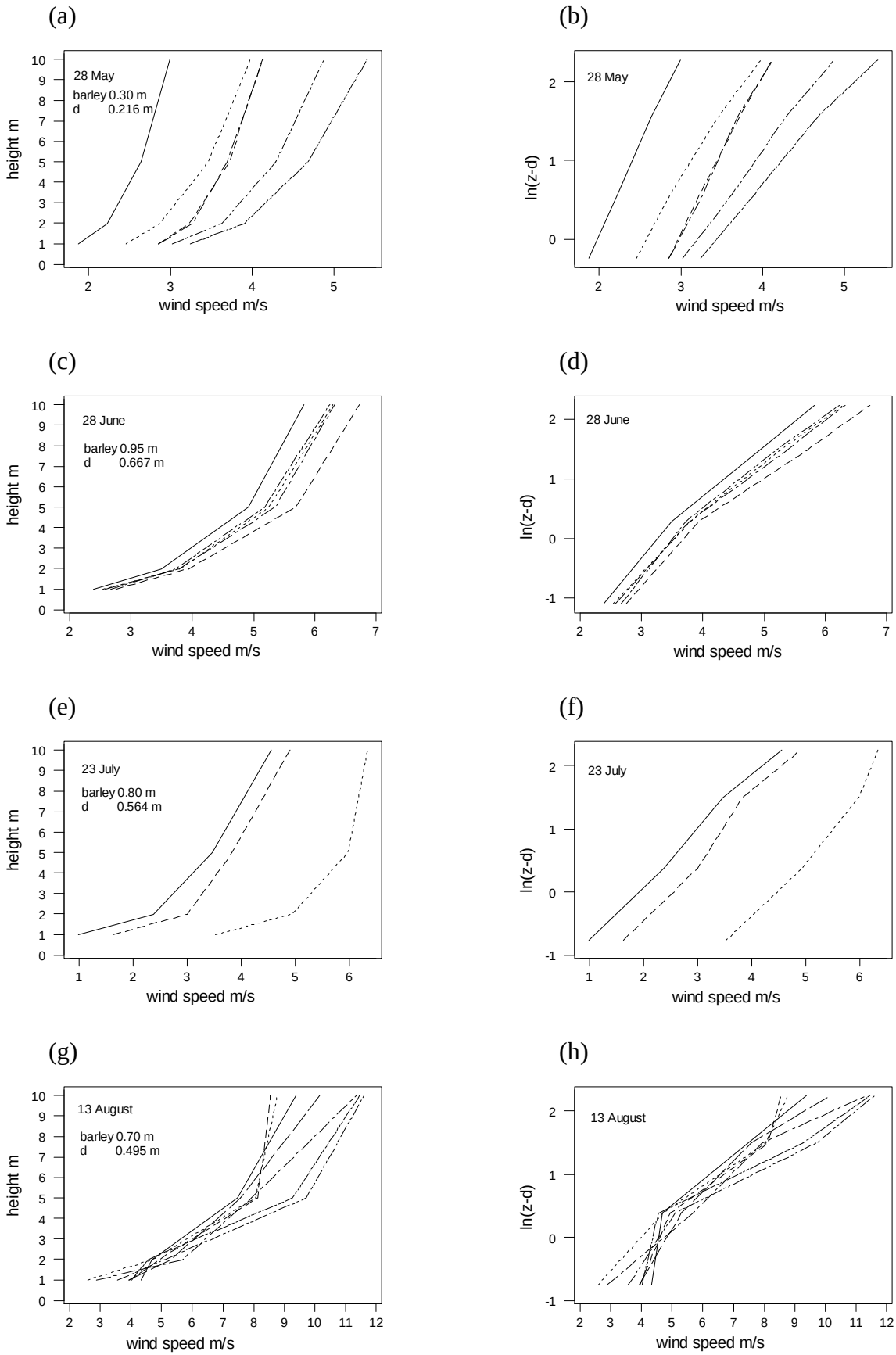

Figure 7.12 (a – h). Wind profiles representing winds above the eastern field, Ilstorp, plotted against height (z) and ln (z-d).

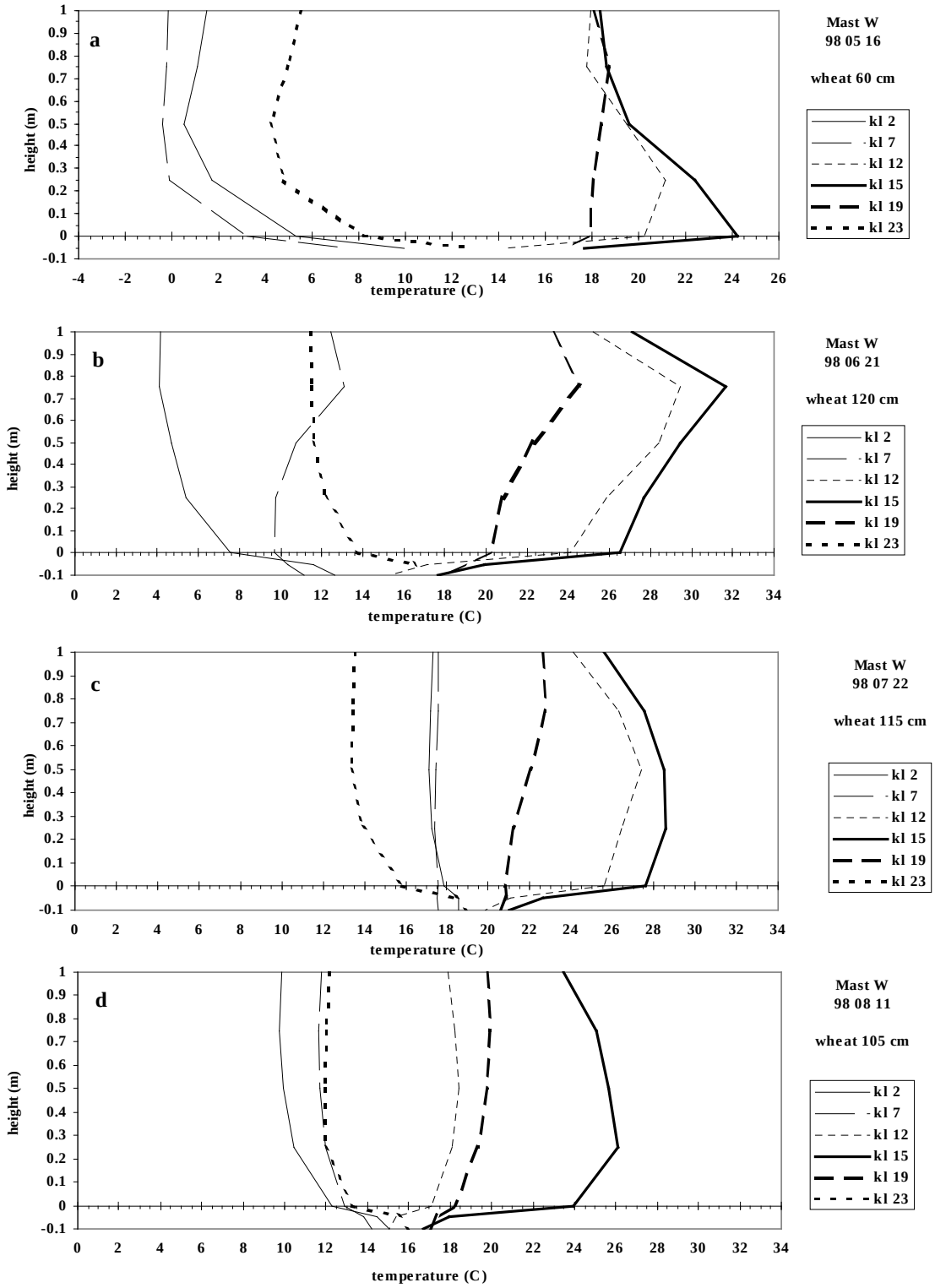

Figure 7.13 (a – d). Temperature profiles in the field of wheat, Ilstorp, on 16th of May, 21st of June, 22nd of July and 11th of August 1998. Selected hourly temperature averages (°C) are plotted against height (m). The increasing crop height is noted for each date; 60 cm, 120 cm, 115 cm and 105 cm respectively. Note that the wheat reached its peak height in early July (130 cm).

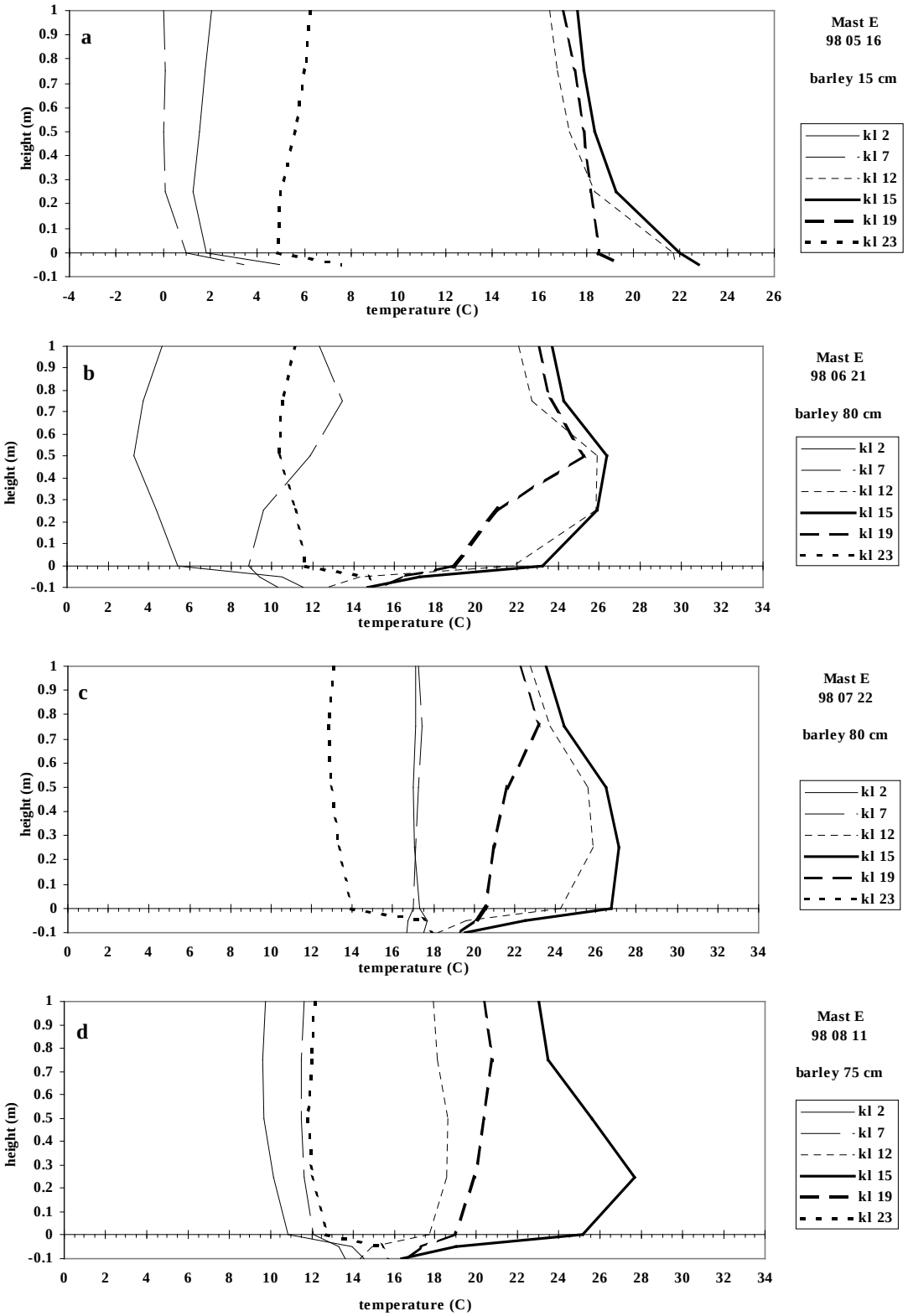

Fig 7.14 (a – d). Temperature profiles in the field of barley, Ilstorp, on 16th of May, 21st of June, 22nd of July and 11th of August 1998. Selected hourly temperature averages (°C) are plotted against height (m). The increasing crop height is noted for each date; 15 cm, 80 cm, 80 cm and 75 cm respectively. Note that the barley reached its peak height in early July (100 cm).

7.5 SURFACE ENERGY BUDGET

7.4.1 Fluxes of net radiation

Net radiation was calculated from input data presented in chapter 6.4.2. In fig 7.15 net radiation has been calculated with three different albedo values. The lower albedo of 18% gives a higher net radiation than calculations involving higher albedos of 23 % to 25 %. Based on this diagram, it was decided to use an albedo of 23% in the net radiation calculations for the whole period.

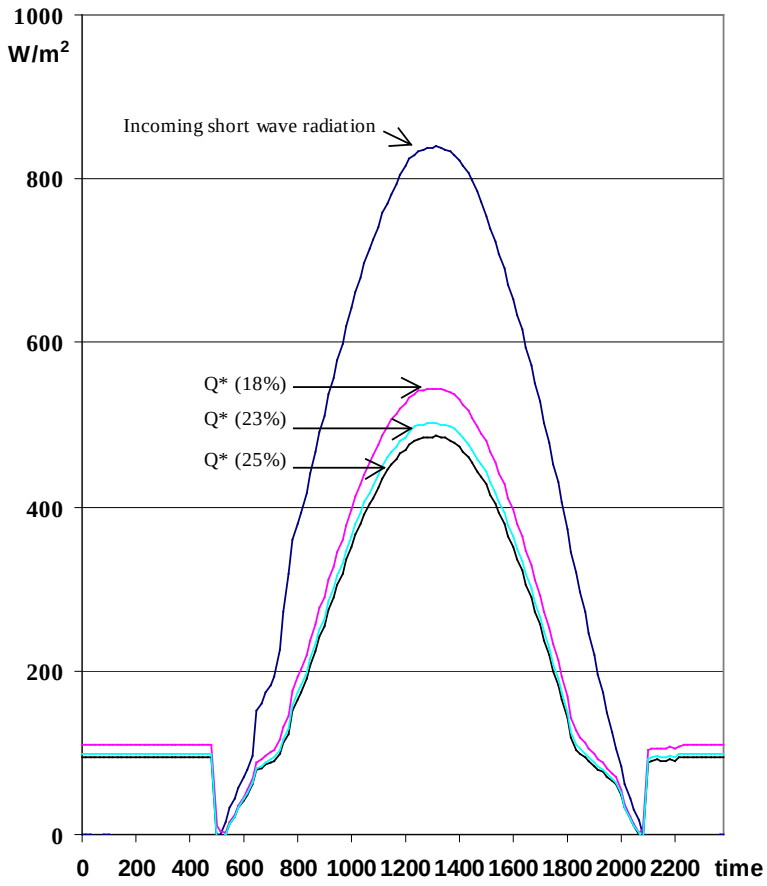

Figure 7.15 Net radiation (Wm^{-2}) calculated for the 16th of May, using albedo values of 18 %, 23 % and 25 %..

7.4.2 Fluxes of sensible heat, latent heat and soil heat

Sensible heat flux was calculated (equation 6.3), and then latent heat flux was obtained by subtracting sensible heat flux and soil heat flux from the net radiation (equation 6.10). The results are displayed in figures 4.16 to 4.19. The fluxes were calculated with input data of wind speed and temperature from the 10 m mast, and represent an average for the two fields.

The soil heat flux was stabilised around 0 – 10 W m^{-2} during the whole period. The sensible heat flux, however, seemed to decrease from May to June, and then gradually increase again in July and August. The latent heat flux increased through the beginning of the summer. In July the flux of latent heat started to decrease, and in August it was below the flux of sensible heat during midday.

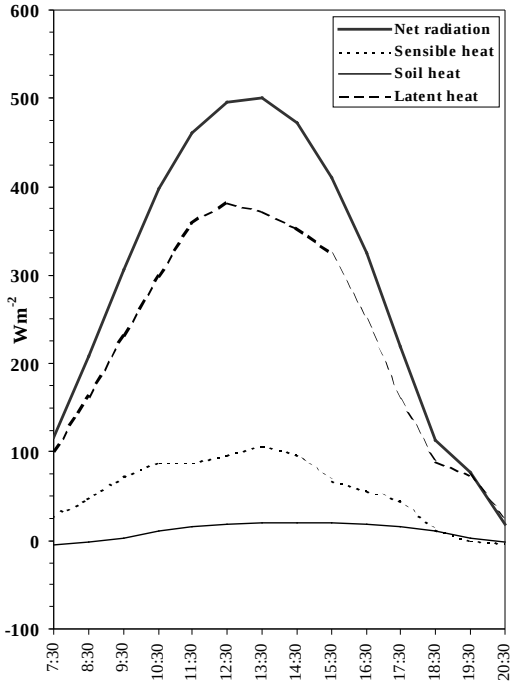

Figure 7.16. Surface energy budget on the 16th of May

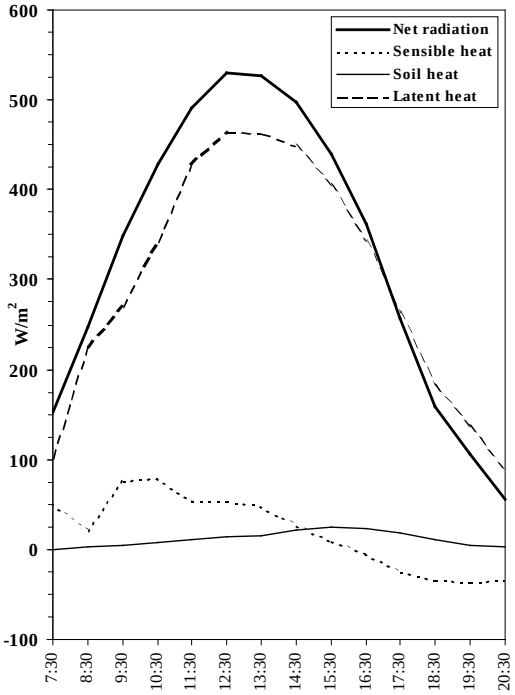

Figure 7.17. Surface energy budget on the 21st of June.

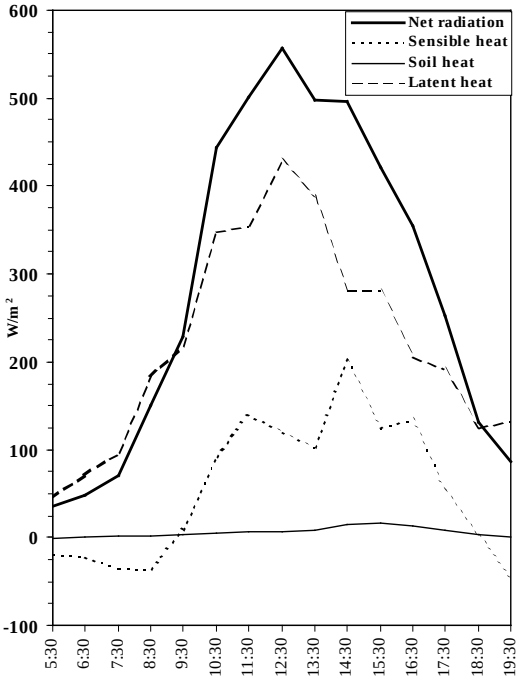

Figure 7.18. Surface energy budget on the 22nd of July.

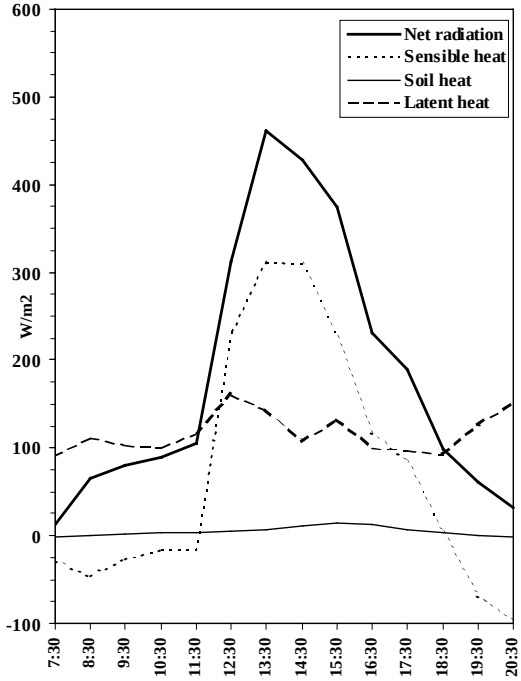

Figure 7.19. Surface energy budget on the 11th of August

8. DISCUSSION

8.1 THE LOGARITHMIC WIND PROFILE AND CROP HEIGHT

As expected the theory of the logarithmic wind profile seems to be applicable to the measurements made at Ilstorp. In general, wind profiles plotted against measurement height show a characteristic smooth logarithmic curve at the beginning of the season, when crop height is low. Most apparent is the wind profile above the barley field in May, figure 7.12 (b) where the logarithmic profile show close to perfect straight lines. The displacement height was then derived to 21.6 cm, and the estimated roughness length was 1.1 cm (table 7.1).

It is possible to see then how increasing crop height effects the logarithmic wind profile. In June, figure 7.12 (d), an evident bend is present. There are a few possible explanations to this distinct bend, which also is seen in figures 7.11 (d), (f) and (h) and figures 7.12 (d) and (h). Firstly, the crop height was close to, or above, 1 meter, which means that the wind speed measurements at 1 m probably was effected, causing the bend in the profile. However, the 10 m mast was positioned in between the fields, which means that the fetch might have been disturbed just around the field border, causing an edge effect.

Secondly, another reason for the curved lines in the logarithmic wind profiles arises from the accuracy of the calculated displacement height. The equation formed by Stanhill (Equation 6.7) involved measurements of crop height only, and hence the wind speed or the age of the crop is not taken into consideration.

The estimations of roughness length from the logarithmic wind profiles, table 7.1, and the roughness lengths calculated for the entire growing season, figure 7.10 (a) and (b), using equation (6.8), do not seem to correlate all that well. An answer to this is that the roughness length does depend on more variables than crop height. In some other studies estimating the roughness length from wind speed measurements at different levels has solved this problem (DeHeer-Amissah et al., 1981.).

Perhaps it is not possible to state that the roughness length should depend on crop height in a linear fashion. Just as in the case of displacement height, the roughness length will be affected by the density (and maturity) of the crop stand, and the wind speed. Attempts have been made to find the variation of z_0 and d by developing a second–order equation (Monteith and Unsworth, 1990) for the ratio between these to parameters and the crop height.

8.2 TEMPERATURE PROFILES IN FIELDS OF GROWING CROP

The summer of 1998 was not a very good summer with reference to sunny days. The gentle increase in maximum solar radiation in figure 7.1 reached its peak in early July at about 1150 W m^{-2}, and then decreased remarkably towards the end of summer. This could be referred to the large amount of cloudy and rainy days in July and August.

The temperature readings for 10 m and 0.5 m respectively in figure 7.4, showed that the temperature in the air further away from the ground deviated less from its average temperature, i. e. had lower amplitude, which could be expected.

Comparing the temperature profiles in figure 7.13 (a – d) with 7.14 (a – d) there are obvious differences in the shapes of the profiles within the two fields. These differences seem to decrease as the crop grows. Looking at the night-to-early-morning temperature profiles in the barley field on the 16th of May, figure 7.14 (a), they demonstrate low temperatures, close to

freezing, above the ground, and slightly warmer down in the ground. At the same time, in the wheat field, the ground is already covered with 0.60 m high crop, which helps keeping the heat near the ground, giving a surface temperature close to 3°C. The active surface has risen to somewhere between 0.25 m and 0.50 m, which also can be seen in figure 7.10 (a). During the course of the day both the temperature in the ground and in the air quickly increases. The warmest period during the day occur at 15.00 in both fields. Notably, in the field of barley, the highest temperature is found in the ground at a depth of 0.05 m. The high ground temperature depends on the spacing of the barley seedlings. They are still only 15 cm high, and spaced in rows with a distance of 10 – 15 cm in between them. As the afternoon proceeds, the temperature in the soil decreases faster than in the air. In general it can be concluded from both graphs on the 16th of May, that the temperature profile is neutral to stable during the night, which changes with the increasing wind speeds during the day to become unstable.

As the wheat increased from 60 cm to 120 cm in the western field the temperature profiles changed accordingly. In figure 7.13 (b) the profiles from noon to evening showed a clear inversion up to 0.80 m. It seems to be the result of a lagged nightly inversion which was not fully developed until mid afternoon. At this date the wheat was still green, standing straight. As the summer proceeded and the wheat matured the crop turned yellow and hung with the axes. Then the temperature profile within the field changed, figure 7.13 (c) and (d). The same pattern was noted in the other field. The amplitude of the temperature variations in the ground was strongly reduced when the crop had reached its mature stage. Comparing these findings with figure 3.5, it looked like the general ground temperature profile has risen above ground up to an active surface – the zero plane displacement height.

8.3 DIURNAL AND SEASONAL VARIATION OF ATMOSPHERIC STABILITY

Atmospheric stability above the Ilstorp site (figure 7.9) shows a distinct diurnal cycle, with stable stratification during the night and neutral to unstable atmospheres during daytime. This is pattern is well documented by other studies, for example Frank and Kocurek (1994), who found that the degree of daytime instability increases in magnitude during the summer, as a result of greater surface heating and insolation. However, in Ilstorp there have been days when the atmosphere has been stable, and no convection has occurred, which is evident from the scatter of points between 06:00 h and 18:00 h, ranging from Ri above 1.00.

The logarithmic wind profile is only valid during neutral atmospheric conditions, occurring when Ri lies between –0.01 and 0.01. Looking at figures 7.8 (a – d) it becomes evident that there is a strong connection between high wind speeds and fully forced convection during neutral conditions. When wind speeds are lower the amount of free convection increases slightly, but the amount of periods of no convection at all is remarkably large. This must mean that with low or no wind speeds, the turbulence ceases and fluxes of energy decrease rapidly.

8.4 FLUXES OF SENSIBLE AND LATENT HEAT

Calculating the fluxes of sensible heat using a gradient-profile method implies an almost ideal world, since the similarity theory is based on highly idealised conditions, which are never strictly satisfied in the atmospheric surface layer. However, it is a simple indirect approach to get reasonable good estimates of the energy fluxes.
In the neutral case, the sensible heat flux calculations should be fairly accurate. However the stability corrections used in unstable and stable atmospheres are intriguing. How come that in a stable condition, with Ri extending above 0.2, indicating no convection, the stability correction factor is great, which leads to large heat flux estimations? With no convection, not that much energy flux occurs.

The equations used for correction has been discussed in the literature (Dyer, 1974, Yaglom, 1977, Monteith and Unsworth, 1990) and perhaps the generalised correction factor, F, used here is simply too general.

8.5 DIURNAL AND SEASONAL VARIATION IN THE ENERGY BALANCE

The calculated energy budgets show results in harmony with the theory. The diurnal variation in energy balance in figures 7.16 – 7.19 follow a cyclic pattern. In general, the latent heat flux and sensible heat flux reached their peak values during mid-day. The sensible heat flux seemed to lag behind the latent heat flux. The soil heat flux reached its peak value first in the afternoon. Proportionately moist soil, due to rainy weather, figure 7.6 and 7.7, in combination with the presence of a low vegetation cover of young, green, growing crop, explains the very dominant role of latent heat flux in the first three figures, indicating a high degree of evaporation. On the 21st of June, figure 7.17, the sensible heat flux even became negative, showing that such a vast amount of the energy available was used for evaporation, that in the afternoon, to maintain the balance, sensible heat was flowing downwards.

The energy budget for the 11th of August showed for the first time higher values for sensible heat flux than latent heat flux during the day. This relates to limited access of water, since the crop successively had matured and dried to become yellow. Notably the amount of latent heat flux was high during morning and afternoon in comparison to net radiation. The same phenomenon is seen in figure 3.4.

Indirectly it is possible to see the increase of the active surface, the zero plane displacement height together with the roughness length, by studying the reciprocal relation between the energy components.

Comparing the results in Ilstorp with other studies in the energy budget above agricultural crop or forest, some similarities show. In the work by Verma *et al.* (1986) regarding fluxes of carbon dioxide, water vapour and sensible heat over a deciduous forest, the diurnal pattern of energy fluxes in August show that maximum values of sensible heat ranged from 150 to 200 W m^{-2}. Latent heat values reached 300 to 350 W m^{-2} at its peak. These findings are well in agreement with the results in Ilstorp. However, in Ilstorp latent heat exchange seem highly correlated with Q*, which is not the case above the forest.

Lagourde and McAneney (1992) have made some work on calculations of sensible heat. They compared sensible heat flux obtained by aerodynamic and eddy correlation methods above a wheat field in Moulés, France. They found that the two methods were compatible, since both methods resulted in a sensible heat flux between 250 – 300 Wm^{-2}. Lagourde and McAneney related the high values of sensible heat flux to periods when water was a limiting factor. The dry, hot conditions enabled sensible heat flux to become a significant component in the surface energy budget.

Sensible heat fluxes in Ilstorp show much lower values in May to July, when it rained a lot. It is not until August the heat flux increased to around 300 W m^{-2}.
Hicks and Wesely (1981) estimated sensible heat flux above maize and soybeans, Illinois, and found that the heat flux peaked at 120 – 150 Wm^{-2}.

In conclusion, possible sources of error should be commented. Possible errors sort under three categories; instruments, fieldwork and data sampling, and theory.
To avoid faults arising from problems with instruments, all instruments were calibrated and adjusted. Further, the radiation shields were of a simpler character, without fans to circulate the air. Possibly this has affected the temperature and humidity measurements. However, one can always wish for better equipment, great weather and an ideal site. This leads us to problems related to fieldwork and data sampling.

A desirable position of the small masts (and of course also the 10 m mast) would have been out in the middle of each field, but due to cultivation methods this was not possible to fulfill completely. Fetch requirements could have been fulfilled to a higher degree if the conifer plantation had been chopped down. Another solution could have been to only use data collected up to a height of 5 m, to be on the totally safe side.

Finally, the theory behind the gradient-profile method relies on several assumptions and ideal states, such as similarity between diffusion coefficients in air at neutral atmospheric conditions etc. which has led to a lot of different correction factors for various sorts of surfaces and atmospheric stabilities. Further, von Karman's constant, k , is an empirical coefficient which can differ from 0.35 to 0.41 in the literature.

The aim with the gradient-profile method has been to try to describe the micro climatological processes involving energy fluxes in a simple way, but perhaps the processes are not so simple. With the evolution of new instruments and new techniques to measure energy fluxes it would be interesting to further develop this study, and correlate the calculations against direct measurements of fluxes.

9. CONCLUSION

In general, the results confirmed the theories outlined. In temperature and wind profiles it was possible to detect a rise in the active surface, the level at which the energy partitioning occurs, which was related to increasing crop height. The use of the logarithmic wind profile made it possible to estimate the actual level of displacement height and roughness length. However, the relation between this active level and crop height was not as simple as predicted.

Using the expression of Gradient Richardson's number showed that atmospheric stability varied both with time of the day, and wind speed.

Despite indirect measures of net radiation, the energy budget above the fields appeared to be in accordance with other similar studies.

REFERENCES

Blennow, K., 1997, *Spatial variation in near-ground radiation and low temperature - Interactions with forest vegetation*, Meddelanden från Lunds Universitets geografiska institutioner, avhandlingar 132, Lund university Press, Lund

Blümel, K., 1998, Estimation of sensible heat flux from surface temperature wave and one-time-of-day air temperature observation, *Boundary-Layer Meteorology*, 86: 193 – 232

Bärring, L., Jönsson, P., Achberger, C., Ekström, M. and Kjellander, C., 1999, WEELS intermediate project report for 1998 from Partner 3, EC-report

Cellier, P., 1986, On the validity of flux-gradient relationships above very rough surfaces, *Boundary-Layer Meteorology*, 36: 417 - 419

Cleugh, H. A. and Oke, T. R., 1986, Suburban-rural energy balance comparisons in summer for Vancouver, B. C., *Boundary-Layer Meteorology* 36: 351 – 369

Daniel, E., 1992, *Description of the quartenary maps Tomelilla SV and Ystad NV*. Swedish geological survey, Uppsala, Serie Ae Nr 99-100, 149 pp.

DeHeer, A., Högström, U. and Smedman-Högström, A., 1981, Calculation of sensible and latent heat fluxes, and surface resistance from profile data, *Boundary-Layer Meteorology*, 20: 35 – 49

Dyer, A. J., 1974, A review of flux-profile relationships, *Boundary-Layer Meteorology*, 7: 363 - 372

Grant, A.L.M., 1994, Wind profiles in the stable boundary layer, and the effect of low relief, *Quart. J. R. Met. Soc.* 120: 27 – 46

Frank, A. and Kocurek, G., 1994, Effects of atmospheric conditions on wind profiles and aeolian sand transport with example from White Sands National Monument, *Earth surface processes and landforms*, 19: 735 – 745

Hicks, B. B. and Wesely, M. L., 1981, Heat and momentum transfer characteristics of adjacent fields of soybeans and maize, *Boundary-Layer Meteorology*, 20: 175 – 185

Huband, N. D. S. and Monteith, J. L., 1986 (a), Radiative surface temperature and energy balance of a wheat canopy I. Comparison of radiative and aerodynamic canopy temperature, *Boundary-Layer Meteorology*, 36: 1 – 17

Huband, N. D. S. and Monteith, J. L., 1986 (b), Radiative surface temperature and energy balance of a wheat canopy II. Estimating fluxes of sensible and latent heat, *Boundary-Layer Meteorology*, 36: 107 – 116

Kaimal, J. C. and Finnigan, J. J., 1994, *Atmospheric boundary layer flows: their structure and measurement*, Oxford University Press Inc, New York, 290 pp

Lagouarde, J. P. and McAneney, K. J., 1992, Daily sensible heat flux estimation from a single measurement of surface temperature and maximum air temperature, *Boundary-Layer Meteorology*, 59: 341 – 362

Lhomme, J.-P., Chehbouni, A. and Monteny, B., 1994, Effective parameters of surface energy balance in heterogeneous landscape, *Boundary-Layer Meteorology*, 71: 297 – 309

Lindroth, A. and Iritz, Z, 1993, Surface energy budget dynamics of short-rotation willow forest, *Theor. Appl. Climatol.*, 47: 175 – 185

Loman, G., 1986, The climate of a sugar beet stand – Dynamics, impact on the crop and possibilities of improvement, Meddelanden från Lunds Universitets Geografiska institution, avhandlingar 101, Lund university Press, Lund

Miller, D. H., 1981, *Energy at the surface of the earth – An introduction to the energetics of ecosystems*, Academic Press, New York, 516 pp

Monteith, J.L. and Unsworth, M., 1990, *Principles of Environmental Physics*, Second edition, Arnold, Hodder Headline Group, London

Mölder, M., 1998, *Roughness lengths and roughness sublayer corrections in partly forested regions*, Acta Universitatis Upsaliensis, Uppsala

Oke, T.R., 1987, *Boundary Layer Climates*, Second edition, Routledge, London, 435 pp

Panofsky, H. A., 1963, Determination of stress from wind and temperature measurements, *Quart. J. R. Met. Soc. 89: 85 – 94*

Rosenberg, N. J., Blad, B. L. and Verma, S. B., 1983, *Microclimate – The biological environment*, Second edition, John Wiley & Sons, New York, 495 pp

Stull, R. B., 1988, *An introduction to boundary layer meteorology*, Kluwer Academic Publishers, Dordrecht, The Netherlands, 666 pp

Stull, R. B., 1995, *Meteorology today for scientists and engineers – A technical companion book*, West Publishing CO, USA,

Thom, A. S., Stewart, J. B., Olivier, H. R. and Gash, J. H. C., 1975, Comparison of aerodynamic and energy budget estimates of fluxes over a pine forest, *Quart. J. R. Met. Soc., 101: 93 – 105*

Trambouze, W., Bertuzzi, P. and Voltz, M., 1998, *Comparison of methods for estimating actual evapotranspiration in a row-cropped vineyard*, Agricultural and Forest Meteorology, 91: 193 – 208

Verma, S. B., Baldocchi, D. D., Anderson, D. E., Matt, D. R. and Clement, R. J., 1986, Eddy fluxes of CO_2, water vapor and sensible heat over a deciduous forest, *Boundary-Layer Meteorology*, 36: 71 – 91

Yaglom, A. M., 1977, Comments on wind and temperature flux-profile relationships, *Boundary-Layer Meteorology*, 11: 89 - 102

Åhman, R., 1974, Vinderosion i Skåne, *Svensk Geografisk Årsbok*, vol 50: 232 - 240

Appendix A1

Temperature and soil heat flux measurements
Ilstorp

```
*Table 1 Program
  01:10    Execution Interval (seconds)                    sampling interval each  10 s

1:  Batt Voltage (P10)                                     battery
 1: 1        Loc [ batteri   ]

2:  Temp (107) (P11)                                       references temperature
 1: 1        Reps
 2: 12       SE Channel
 3: 3        Excite all reps w/Exchan 3
 4: 2        Loc [ reftemp   ]
 5: 1.0      Mult
 6: 0.0      Offset

3:  Volt (Diff) (P2)                                       heat flow sensor, 4 st
 1: 4        Reps
 2: 1        2.5 mV Slow Range
 3: 2        DIFF Channel
 4: 3        Loc [ flow_1    ]
 5: 500    Mult
 6: 0.0      Offset

4:  Set Port(s) (P20)                                      multiplexor
 1: 0000     C8,C7,C6,C5 Options
 2: 0051     C4..C1 = low/low/100ms/high

5:  Beginning of Loop (P87)
 1: 0000     Delay
 2: 10       Loop Count

6:  Do (P86)
 1: 72       Pulse Port 2

7:  Thermocouple Temp (DIFF) (P14)                         thermocouples, 14 st
 1: 1        Reps
 2: 1        2.5 mV Slow Range
 3: 01       DIFF Channel
 4: 1        Type T (Copper-Constantan)
 5: 2        Ref Temp Loc [ reftemp   ]
 6: 7     -- Loc [ temp_1    ]
 7: 1.0      Mult
 8: 0.0      Offset

8:  End (P95)

9:  Beginning of Loop (P87)
 1: 0000     Delay
2: 1        Loop Count

10:  Do (P86)
 1: 72       Pulse Port 2
```

```
11:  Volt (Diff) (P2)                          reflected short wave radiation
 1: 1        Reps                              Kipp & Zonen
 2: 3        25 mV Slow Range
 3: 1        DIFF Channel
 4: 21       Loc [ rad       ]                 Not connected!
 5: 72.886   Mult
 6: 0.0      Offset

12:  End (P95)

13:  Set Port(s) (P20)
 1: 0000     C8,C7,C6,C5 Options
 2: 0090     C4..C1 = low/low/nc/low

14:  If time is (P92)                          averages for each
 1: 0000     Minutes (Seconds --) into a       10 min period
 2: 10       Interval (same units as above)
 3: 10       Set Output Flag High

15:  Real Time (P77)
 1: 1110     Year,Day,Hour/Minute (midnight = 0000)

16:  Average (P71)                             reference temperature - average
 1: 1        Reps
 2: 2        Loc [ reftemp   ]

17:  Average (P71)                             heat flow sensors -averages
 1: 4        Reps
 2: 3        Loc [ flow_1    ]

18:  Average (P71)                             temperature + refl radiation - average
 1: 15       Reps
 2: 7        Loc [ temp_1    ]

19:  Serial Out (P96)                          storage module  - SM 192
 1: 71       SM192/SM716/CSM1

*Table 2 Program
  02: 0.0000    Execution Interval (seconds)

*Table 3 Subroutines

End Program
```

Appendix A2

Calibration of thermocouples
Ilstorp

```
*Table 1 Program
  01: 1        Execution Interval (seconds)

1:  Batt Voltage (P10)
 1: 1        Loc [ batteri   ]

2:  Temp (107) (P11)
 1: 1        Reps
 2: 12       SE Channel
 3: 3        Excite all reps w/Exchan 3
 4: 2        Loc [ reftemp   ]
 5: 1.0      Mult
 6: 0.0      Offset

3:  Set Port(s) (P20)
 1: 0000     C8,C7,C6,C5 Options
 2: 0051     C4..C1 = low/low/100ms/high

4:  Beginning of Loop (P87)
 1: 0000     Delay
 2: 10       Loop Count

5:  Do (P86)
 1: 72       Pulse Port 2

6:  Thermocouple Temp (DIFF) (P14)
 1: 1        Reps
 2: 1        2.5 mV Slow Range
 3: 1        DIFF Channel
 4: 1        Type T (Copper-Constantan)
 5: 2        Ref Temp Loc [ reftemp   ]
 6: 3     -- Loc [ tempe_1   ]
 7: 1.0      Mult
 8: 0.0      Offset

7:  End (P95)

8:  Set Port(s) (P20)
 1: 0000     C8,C7,C6,C5 Options
 2: 0090     C4..C1 = low/low/nc/low

9:  If time is (P92)
 1: 0000     Minutes (Seconds --) into a
 2: 1        Interval (same units as above)
 3: 10       Set Output Flag High

10:  Real Time (P77)
 1: 110      Day,Hour/Minute (midnight = 0000)

11:  Average (P71)
 1: 10       Reps
 2: 3        Loc [ tempe_1   ]
```

12: Maximize (P73)
 1: 10   Reps
 2: 0   Value Only
 3: 3   Loc [tempe_1   ]

13: Minimize (P74)
 1: 10   Reps
 2: 0   Value Only
 3: 3   Loc [tempe_1   ]

*Table 2 Program
 02: 0.0000   Execution Interval (seconds)

*Table 3 Subroutines

Appendix B

List of symbols

Symbol	SI Unit	Quantity
α		albedo
ε		surface emissivity
σ	W m^{-2} K^{-4}	Stefan-Boltzmann constant
ρ	Kg m^{-3}	air density
τ	Pa	surface shearing stress, flux of momentum
Γ	K m^{-1}	dry adiabatic lapse rate
θ	K	potential temperature
ρ_v	g m^{-3}	absolute humidity
$\mathbf{C_a}$	J m^{-3} K^{-1}	heat capacity of air
d	m	zero plane displacement height
F		generalised stability factor
g	m s^{-2}	gravity
h	m	crop height
k		von Karman's constant
$\mathbf{K\downarrow}$	W m^{-2}	incoming short wave radiation
$\mathbf{K\uparrow}$	W m^{-2}	reflected short wave radiation
K*	W m^{-2}	net short wave radiation
$\mathbf{K_C}$	m^2 s^{-1}	eddy diffusion coefficient (carbon dioxide)
$\mathbf{K_H}$	m^2 s^{-1}	eddy diffusion coefficient – eddy conductivity (heat)
$\mathbf{K_M}$	m^2 s^{-1}	eddy diffusion coefficient – eddy viscosity (momentum)
$\mathbf{k_s}$	W m^{-1} K^{-1}	thermal conductivity
$\mathbf{K_V}$	m^2 s^{-1}	eddy diffusion coefficient (water vapour)
$\mathbf{L\uparrow}$	W m^{-2}	emitted long wave radiation from the earth
$\mathbf{L\downarrow}$	W m^{-2}	incoming long wave radiation from clouds and particles
L*	W m^{-2}	net long wave radiation
$\mathbf{L_v}$	J kg^{-1}	latent heat of vapourization
$\mathbf{Q\uparrow}$	W m^{-2}	radiation leaving the earth surface
$\mathbf{Q\downarrow}$	W m^{-2}	radiation incident on the earth surface
Q*	W m^{-2}	net radiation
$\mathbf{Q_E}$	W m^{-2}	latent heat
$\mathbf{Q_G}$	W m^{-2}	heat conduction in the soil
$\mathbf{Q_H}$	W m^{-2}	sensible heat
$\mathbf{R_C}$		critical Richardson's number
Ri		gradient Richardson's number
$\mathbf{R_T}$		termination of turbulence based on Richardson's Number
T	K	temperature
$\mathbf{T_s}$	K	soil temperature
u	m s^{-1}	wind velocity
$\mathbf{u_*}$	m s^{-1}	friction velocity
z	m	instrument height
$\mathbf{z_0}$	m	roughness length

Lunds Universitets Naturgeografiska institution. Seminarieuppsatser. Uppsatserna finns tillgängliga på Naturgeografiska institutionens bibliotek, Sölvegatan 13, 223 62 LUND.

The reports are available at the Geo-Library, Department of Physical Geography, University of Lund, Sölvegatan 13, S-223 62 Lund, Sweden.

1. Pilesjö, P. (1985): Metoder för morfometrisk analys av kustområden.
2. Ahlström, K. & Bergman, A. (1986): Kartering av erosionskänsliga områden i Ringsjöbygden.
3. Huseid, A. (1986): Stormfällning och dess orsakssamband, Söderåsen, Skåne.
4. Sandstedt, P. & Wällstedt, B. (1986): Krankesjön under ytan - en naturgeografisk beskrivning.
5. Johansson, K. (1986): En lokalklimatisk temperaturstudie på Kungsmarken, öster om Lund.
6. Estgren, C. (1987): Isälvsstråket Djurfälla-Flädermo, norr om Motala.
7. Lindgren, E. & Runnström, M. (1987): En objektiv metod för att bestämma läplanteringars läverkan.
8. Hansson, R. (1987): Studie av frekvensstyrd filtringsmetod för att segmentera satellitbilder, med försök på Landsat TM-data över ett skogsområde i S. Norrland.
9. Matthiesen, N. & Snäll, M. (1988): Temperatur och himmelsexponering i gator: Resultat av mätningar i Malmö.

10A. Nilsson, S. (1988): Veberöd. En beskrivning av samhällets och bygdens utbyggnad och utveckling från början av 1800-talet till vår tid.

10B. Nilson, G., 1988: Isförhållande i södra Öresund.

11. Tunving, E. (1989): Översvämning i Murciaprovinsen, sydöstra Spanien, november 1987.
12. Glave, S. (1989): Termiska studier i Malmö med värmebilder och konventionell mätutrustning.
13. Mjölbo, Y. (1989): Landskapsförändringen - hur skall den övervakas?
14. Finnander, M-L. (1989): Vädrets betydelse för snöavsmältningen i Tarfaladalen.
15. Ardö, J. (1989): Samband mellan Landsat TM-data och skogliga beståndsdata på avdelningsnivå.
16. Mikaelsson, E. (1989): Byskeälvens dalgång inom Västerbottens län. Geomorfologisk karta, beskrivning och naturvärdesbedömning.
17. Nhilen, C. (1990): Bilavgaser i gatumiljö och deras beroende av vädret. Litteraturstudier och mätning med DOAS vid motortrafikled i Umeå.
18. Brasjö, C. (1990): Geometrisk korrektion av NOAA AVHRR-data.
19. Erlandsson, R. (1991): Vägbanetemperaturer i Lund.
20. Arheimer, B. (1991): Näringsläckage från åkermark inom Brååns dräneringsområde. Lokalisering och åtgärdsförslag.
21. Andersson, G. (1991): En studie av transversalmoräner i västra Småland.

22A. Skillius, Å., (1991): Water havesting in Bakul, Senegal.

22B. Persson, P. (1991): Satellitdata för övervakning av höstsådda rapsfält i Skåne.

23. Michelson, D. (1991): Land Use Mapping of theThat Luang - Salakham Wetland, Lao PDR, Using Landsat TM-Data.
24. Malmberg, U. (1991): En jämförelse mellan SPOT- och Landsatdata för vegetationsklassning i Småland.
25. Mossberg, M. & Pettersson, G. (1991): A Study of Infiltration Capacity in a Semiarid Environment, Mberengwa District, Zimbabwe.
26. Theander, T. (1992): Avfallsupplag i Malmöhus län. Dränering och miljöpåverkan.
27. Osaengius, S. (1992): Stranderosion vid Löderups strandbad.
28. Olsson, K. (1992): Sea Ice Dynamics in Time and Space. Based on upward looking sonar, satellite images and a time series of digital ice charts.
29. Larsson, K. (1993): Gully Erosion from Road Drainage in the Kenyan Highlands. A Study of Aerial Photo Interpreted Factors.
30. Richardson, C. (1993): Nischbildningsprocesser - en fältstudie vid Passglaciären, Kebnekaise.
31. Martinsson, L. (1994): Detection of Forest Change in Sumava Mountains, Czech Republic Using Remotely Sensed Data.
32. Klintenberg, P. (1995): The Vegetation Distribution in the Kärkevagge Valley.
33. Hese, S. (1995): Forest Damage Assessment in the Black Triangle area using Landsat TM, MSS and Forest Inventory data.
34. Josefsson, T. och Mårtensson, I. (1995). A vegetation map and a Digital Elevation Model over the Kapp Linné area, Svalbard -with analyses of the vertical and horizontal distribution of the vegetation
35. Brogaard, S och Falkenström, H. (1995). Assessing salinization, sand encroachment and expanding

urban areas in the Nile Valley using Landsat MSS data.
36. Krantz, M. (1996): GIS som hjälpmedel vid växtskyddsrådgivning.
37. Lindegård, P. (1996). VINTERKLIMAT OCH VÅRBAKSLAG. Lufttemperatur och kådflödessjuka hos gran i södra Sverige.
38. Bremborg, P. (1996). Desertification mapping of Horqin Sandy Land, Inner Mongolia, by means of remote sensing.
39. Hellberg, J. (1996). Förändringsstudie av jordbrukslandskapet på Söderslätt 1938-1985.
40. Achberger, C. (1996): Quality and representability of mobile measurements for local climatological research.
41. Olsson, M. (1996): Extrema lufttryck i Europa och Skandinavien 1881-1995
42. Sundberg, D. (1997): En GIS-tillämpad studie av vattenerosion i sydsvensk jordbruksmark.
43. Liljeberg, M. (1997): Klassning och statistisk separabilitetsanalys av marktäckningsklasser i Halland, analys av multivariata data Landsat TM och ERS-1 SAR.
44. Roos, E. (1997): Temperature Variations and Landscape Heterogeneity in two Swedish Agricultural Areas. An application of mobile measurements.
45. Arvidsson, P. (1997): Regional fördelning av skogsskador i förhållande till mängd SO_2 under vegetationsperioden i norra Tjeckien.
46. Akselsson, C. (1997): Kritisk belastning av aciditet för skogsmark i norra Tjeckien.
47. Carlsson, G. (1997): Turbulens och supraglacial meandring.
48. Jönsson, C. (1998): Multitemporala vegetationsstudier i nordöstra Kenya med AVHRR NDVI
49. Kolmert, S. (1998): Evaluation of a conceptual semi-distributed hydrological model – A case study of Hörbyån.
50. Persson, A. (1998): Kartering av markanvändning med meteorologisk satellitdata för förbättring av en atmosfärisk spridningsmodell.
51. Andersson, U. och Nilsson, D. (1998): Distributed hydrological modelling in a GIS perspective – an evaluation of the MIKE SHE model.
52. Andersson, K. och Carlstedt, J. (1998): Different GIS and remote sensing techniques for detection of changes in vegetation cover - A study in the Nam Ngum and Nam Lik catchment areas in the Lao PDR.
53. Andersson, J., (1999): Användning av global satllitdata för uppskattning av spannmålsproduktion i västafrikanska Sahel.
54. Flodmark, A.E., (1999): Urban Geographic Information Systems, The City of Berkeley Pilot GIS
55. Tagesson, I., och Wramneby, A., (1999): Kväveläckage inom Tolångaåns dräneringsområde – modellering och åtgärdssimulering.
56. Almkvist, E., (1999): Högfrekventa tryckvariationer under de senaste århundradena.
57. Alstorp, P., och Johansson, T., (1999): Översiktlig buller- och luftföroreningsinventering i Burlövs Kommun år 1994 med hjälp av geografiska informationssystem – möjligheter och begränsningar.
58. Mattsson, F., (1999): Analys av molnklotter med IRST-data inom det termala infraröda våglängdsområdet
59. Hallgren, L., och Johansson, A., (1999): Analysing land cover changes in the Caprivi Strip, Namibia, using Landsat TM and Spot XS imagery.
60. Granhäll, T., (1999): Aerosolers dygnsvariationer och långväga transporter.
61. Kjellander, C., (1999): Variations in the energy budget above growing wheat and barley, Ilstorp 1998 – a gradient-profile approach
62. Moskvitina, M., (1999): GIS as a Tool for Environmental Impact Assessment - A case study of EIA implementation for the road building project in Strömstad, Sweden